

DAO: A New and Public Non-Relativistic Reflection Model

YIMIN HUANG ,¹ HONGHUI LIU ,^{2,*} COSIMO BAMBI ,^{1,3,†} ADAM INGRAM ,⁴ JIACHEN JIANG ,⁵
 ANDREW YOUNG ,⁶ AND ZUOBIN ZHANG ,⁷

¹Center for Astronomy and Astrophysics, Center for Field Theory and Particle Physics and
 Department of Physics, Fudan University, Shanghai 200438, China

²Institut für Astronomie und Astrophysik, Eberhard-Karls Universität Tübingen, D-72076 Tübingen, Germany

³School of Humanities and Natural Sciences, New Uzbekistan University, Tashkent 100001, Uzbekistan

⁴School of Mathematics, Statistics, and Physics, Newcastle University, Newcastle upon Tyne NE1 7RU, UK

⁵Department of Physics, University of Warwick, Gibbet Hill Road, Coventry CV4 7AL, UK.

⁶H.H. Wills Physics Laboratory, Tyndall Avenue, Bristol BS8 1TL, UK

⁷Astrophysics, Department of Physics, University of Oxford, Keble Road, Oxford OX1 3RH, UK

ABSTRACT

We present a new non-relativistic reflection model, DAO, designed to calculate reflection spectra in the rest frame of accretion disks in X-ray binaries and active galactic nuclei. The model couples the XSTAR code, which treats atomic processes, with the Feautrier method for solving the radiative transfer equation. A key feature of DAO is the incorporation of a high-temperature corrected cross section and an exact redistribution function to accurately treat Compton scattering. Furthermore, the model accommodates arbitrary illuminating spectra, enabling applications across diverse physical conditions. We investigate the spectral dependence on key physical parameters and benchmark the results against the widely used `reflionx` and `xillver` codes.

Keywords: High energy astrophysics (739); X-ray binaries (1811); AGN (16); Atomic physics (2063); Radiative transfer (1335)

1. INTRODUCTION

The X-ray spectra of X-ray binary systems (XRBs) and active galactic nuclei (AGNs) are essential for understanding the process of accretion onto black holes (BHs). These spectra typically consist of several components: (1) thermal emission from a geometrically thin and optically thick accretion disk (Shakura & Sunyaev 1973; Novikov & Thorne 1973); (2) non-thermal emission from a hot corona (\sim 100 keV), whose spectrum follows a power-law-like shape with a high-energy cut-off (Thorne & Price 1975; Shapiro et al. 1976; Zdziarski et al. 1995); and (3) reprocessed coronal emission from the accretion disk, commonly referred to as the reflection component (Tanaka et al. 1995; Risaliti et al. 2013; Bambi et al. 2021). The reflection spectrum encodes information about the disk properties (e.g., density, ionization state, and elemental abundances) as well as the spacetime geometry near the central black hole (Fabian

et al. 1989; George & Fabian 1991; Ballantyne et al. 2001; García & Kallman 2010; Dauser et al. 2010; Tripathi et al. 2019b,a, 2021). Modeling the reflection spectrum and fitting it to the data is particularly useful for extracting this information (Bambi et al. 2021; Reynolds 2021; Liu et al. 2023a,b; Draghis et al. 2024).

Calculating the disk reflection spectrum involves two steps: (1) computing the reflection spectrum in the local rest frame by solving the radiative transfer equation, taking into account processes such as photoionization and Compton scattering (George & Fabian 1991; García & Kallman 2010); and (2) integrating the local reflection spectrum from the inner to the outer disk while including all relativistic effects, such as light bending, Doppler shifts, and gravitational redshift (Fabian et al. 1989; Dauser et al. 2010; Liu et al. 2025; Huang et al. 2025). Integration can be done based on a standard pre-tabulated transfer function (see Bambi 2024, for more details).

* honghui.liu@uni-tuebingen.de

† bambi@fudan.edu.cn

For the rest-frame reflection spectrum, `reflionx`⁸ (Ross et al. 1978; Ross & Fabian 1993; Ballantyne et al. 2001; Ross & Fabian 2005, 2007) and `xillver`⁹ (García & Kallman 2010; García et al. 2011, 2013) are the most widely used models in X-ray reflection data analysis. Another code, `TITAN` (Dumont et al. 2003), is also used in the literature. The main difference between them lies in the treatment of atomic physics and radiative transfer. `xillver` adopts the Feautrier method for solving the radiative transfer equation, allowing the calculation of emergent spectra at different viewing angles. It also includes fluorescent lines that are missing in `reflionx` and `TITAN`, due to the powerful atomic database of `XSTAR` (Kallman & Bautista 2001). In addition, `TITAN` only includes Compton heating and cooling in the energy balance, without accounting for Comptonization in the redistribution of photon energy (Dumont et al. 2000). Both `reflionx` and `xillver` treat Compton scattering using the same Gaussian-approximated redistribution function, which is only valid to describe the energy redistribution for low-energy photons ($E_{\text{ph}} \ll m_e c^2$) scattered by low-temperature electron clouds ($kT_e \ll E_{\text{ph}}$).

Energy redistribution in the Compton scattering process should be described by the full quantum-mechanical treatment, and the electrons in hot plasma should follow a relativistic Maxwellian distribution (Nagirner & Poutanen 1993). For scattering of low-energy photons by a low-temperature electron population, both the Gaussian and exact redistribution functions maintain nearly symmetric profiles. In other cases, the energy-exchange probabilities of photons differ markedly between the two formulations (see Appendix B). García et al. (2020) investigated this effect on the reflection spectrum, but it has not yet been implemented in the `xillver` table model. They compared the spectrum calculated with the exact Compton scattering kernel with the publicly available `xillver` table and the Monte Carlo model `pextrav` (Magdziarz & Zdziarski 1995). The results demonstrate that the commonly used approximations for Compton scattering can lead to significant deviations in the high-energy band.

In addition, Poutanen et al. (2018) reported a noticeable discrepancy above 30 keV when comparing `xillverCp` with `pextrav`/`pextriv`. They attributed this difference to the fact that `xillverCp` does not account for the Klein–Nishina effect, which effectively absorbs part of the energy of the incident photons at $E \gtrsim 50$ keV (Zdziarski et al. 2003).

In this paper, we present a new non-relativistic reflection model, `DAO`. The model employs the latest version of the photoionization code `XSTAR` v2.59, to compute atomic processes, thermal equilibrium, and ionization balance, and incorporates the Feautrier method to solve the radiative transfer. It includes the exact redistribution function for Compton scattering as explained in García et al. (2020). We adopt a constant-density gas with a specified column density under a plane-parallel geometry and azimuthal symmetry. The model is open source and designed to be highly flexible, allowing users to adjust nearly all parameters. `DAO` is available on GitHub¹⁰ and Zenodo (Huang et al. 2025).

The manuscript is organized as follows. In Section 2, we introduce the methodology of our model (radiative transfer, iteration process, etc.). The default configuration, as detailed in Section 2.1, is adopted throughout this work unless otherwise specified. In Section 3, we present a comparative analysis of our model against `reflionx` and `xillver`. We also investigate the impact of various parameters, such as the ionization parameter, incident spectrum, incidence angle, and hydrogen density, on the final reflection spectrum. Finally, Section 4 summarizes our findings and outlines future research directions.

2. METHOD

2.1. Basic setup

We consider a constant density slab illuminated from above and below. The slab represents the disk atmosphere, and the illumination from above represents emission from the corona irradiating the disk atmosphere, at an incidence angle θ_i . `DAO` provides several standard forms for the incident spectrum, including a power law, a power law with a high-energy cutoff, the thermal Comptonisation model `nthComp` (Zdziarski et al. 1996), and a blackbody. For the exponentially cut off power law, the specific intensity is given by¹¹

$$I(E) = AE^{1-\Gamma} \exp(-E/E_{\text{cut}}) \quad (1)$$

and the `nthcomp` spectrum is parameterised by Γ , the seed photon temperature kT_{seed} (hardwired to 0.1 keV for a multi-temprature seed photon spectrum), and the electron temperature kT_E . These spectral forms have been widely used in the analysis of data from accreting black holes and neutron stars. Physical processes such as returning radiation and Comptonization can further modify the shape of the illumination (Życki et al.

⁸ https://github.com/honghui-liu/reflionx_tables

⁹ <https://www.sternwarte.uni-erlangen.de/~dauser/research/relxill/>

¹⁰ <https://github.com/ABHModels/DAO>

¹¹ Note that our standard power law form does not include the 0.1 keV cut off that is adopted in `xillver`.

Name	Description	Default	Unit
Grids and maximum iteration steps			
N_{main}	Maximum steps of main iteration loop	15	-
N_{RTE}	Maximum steps of radiative transfer iteration loop	100	-
N_{τ}	Number of depth grid points	200	-
N_E	Number of energy grid points	5000	-
N_{μ}	Number of angle grid points	10	-
Plasma			
$\log \xi$	Ionization parameter	3.0	erg cm s^{-1}
n_h	Hydrogen density	10^{15}	cm^{-3}
A_{Fe}	Iron abundance	Solar	-
T_i	Initial gas temperature	10^6	K
N_{iT}	Iterations for thermal equilibrium	99	-
Illumination			
I_{type}	Incident radiation field type	Power-law	-
$\Gamma/kT_{\text{bb}}^{\text{top}}$	Photon index / Blackbody temperature	2.0	- / eV
E_{cut}/kT_E	High energy cutoff / Electron temperature (nthcomp)	3×10^5	eV
kT_{seed}	Seed photon temperature (nthcomp)	0.1*	keV
μ_{in}	Incident angle ($\cos \theta$)	0.7	-
B_{sw}	Bottom illumination switch	Off	-
frac	Ratio of top flux to total flux	1	-
kT_{bb}	Bottom blackbody temperature	350	eV
File paths			
P_{sca}	Redistribution function	Eq. B13	-
P_{inci}	User-defined incident spectrum (if $I_{\text{type}} = \text{file}$)	-	-
P_{atom}	Atomic database	data	-
P_{out}	Output directory	-	-

Table 1. Model parameters and their units. An asterisk (*) denotes a fixed parameter.

1999; Riaz et al. 2021; Dauser et al. 2022; Mirzaev et al. 2024b,a). To enable broader exploration of physical scenarios, DAO also allows user-defined incident spectra. The incident spectrum at the upper boundary is normalised by the ionization parameter (Tarter et al. 1969)

$$\xi = \frac{4\pi F_x}{n_h}, \quad (2)$$

where F_x is the illuminating X-ray flux¹² and n_h is the hydrogen number density.

DAO includes the option to incorporate a blackbody radiation source at the lower boundary, corresponding to the illumination of the disk atmosphere by thermal emission from the disk midplane. This feature is crucial for XRBs, as their accretion disks can be sufficiently hot to produce strong ionizing radiation (Liu et al. 2023b). A similar boundary condition is implemented in `reflionx`

(Ross & Fabian 2007). At present, such bottom illumination is currently not included in the `xillver` table model. Therefore, to facilitate a direct comparison, we set the lower boundary condition to zero in this work.

Table 1 lists the input parameters of the DAO model. These parameters are grouped into four categories: (1) model grids and maximum iteration steps, (2) initial plasma conditions, (3) boundary illumination, and (4) required file paths.

The grid-related parameters define the discretization of energy, angle, and optical depth, as well as the maximum number of iteration steps. In this work, we adopt 10 linearly spaced cosine-angle bins ranging from 0.05 to 0.95 for the angular quadrature. For the remaining dimensions, a Thomson optical-depth grid consisting of 200 points logarithmically spaced from 10^{-4} to 10 is used, together with a default energy grid of 5000 points covering the range from 0.1 eV to 1000 keV. The maximum number of main iteration steps, N_{main} , and radiative-transfer iteration steps are set to 15 and 200, respectively. These values are sufficient to ensure con-

¹² Our model calculates F_x in the range of 0.1-1000 keV, such as `xillver` (García et al. 2022) but different from `reflionx`, which defines F_x from 0.0013 to 1000 keV

vergence of the model, as discussed in detail in Section 2.4.

Regarding the plasma parameters, **DAO** assigns strictly non-zero default abundances to H, He, C, O, Ne, Mg, Si, S, Ar, Ca, Fe, and Ni. Nevertheless, the abundances of all elements from H to Zn can be freely modified by the user. In practice, we vary only the iron abundance, while keeping all other elemental abundances fixed at solar abundance. Consequently, only the iron abundance, A_{Fe} , is listed in Table 1.

The file-path parameters specify the locations of the pre-calculated Compton scattering redistribution functions, user-defined incident spectra, the atomic database, and the output files. The atomic database employed in **DAO** is the same as that used by **XSTAR**¹³. The output paths correspond to four files that store, respectively, the final temperature profile; ion populations and heating–cooling rates at each depth; the emergent intensity from μ_1 to μ_{N_μ} ; and the mean intensity and illumination.

2.2. Radiative transfer equation

This section outlines the methodology employed in our reflection model **DAO**. We employ **XSTAR** v2.59 (Kallman et al. 2021) to treat the relevant atomic processes, and adopt the Feautrier method (hereafter FTM) (Mihalas 1978; Hubeny & Mihalas 2015) to iteratively solve the radiative transfer equation.

We consider a plane-parallel atmosphere. Under this assumption, the radiative transfer equation can be written as:

$$\mu \frac{\partial I(z, \mu, E)}{\partial \tau(E)} = S(z, \mu, E) - I(z, \mu, E) \quad (3)$$

where the cosine of the angle between the photon propagation direction and the disk normal, μ , and the photon energy, E , define the grids that characterize the radiation field quantities: the specific intensity, I , and the source function, S . The monochromatic optical depth at energy E is

$$d\tau(E) = -\chi(E)dz \quad (4)$$

where z [cm] denotes the height of each layer, and $\chi(E)$ [cm⁻¹] = $\alpha(E) + \alpha^c(E)$, with α^c and α being the scattering and absorption coefficients, respectively.

FTM is based on the solution of the second-order radiative transfer equation (Schuster 1905), which is derived by considering two rays propagating in opposite directions, denoted by $\pm\mu$. From these, we define the mean-like intensity at depth z and in the range

$0 \leq \mu \leq 1$ as

$$u(z, \mu, E) = \frac{1}{2} [I(z, +\mu, E) + I(z, -\mu, E)], \quad (5)$$

and the flux-like intensity as

$$h(z, \mu, E) = \frac{1}{2} [I(z, +\mu, E) - I(z, -\mu, E)]. \quad (6)$$

By adding and subtracting Eq. 3 for $+\mu$ and $-\mu$, we obtain the transfer equations for h and u . Substituting the equation for u into that for h , using the Thomson optical depth ($\tau_T = \int n_e \sigma_T dz$, where $\sigma_T = 6.652 \times 10^{-25}$ cm² is the Thomson scattering cross section) to define the depth grid, and abbreviating the notation, we obtain the second-order radiative transfer equation:

$$\mu^2 \frac{\partial^2 u(\mu, E)}{\partial \tau^2(E)} = u(\mu, E) - S(E) \quad (7)$$

A key assumption in this equation is the forward–backward symmetry of the source function¹⁴, i.e., $S(+\mu) = S(-\mu)$. This symmetry is essential for solving the second-order radiative transfer equation (Eq. 7) using the FTM. When this approximation is not valid, alternative methods must be employed (Milkey et al. 1975). The source function can then be expressed as

$$S(E) = \frac{j(E)}{\alpha^c(E) + \alpha(E)} + \frac{\alpha^c(E)J^c(E)}{\alpha^c(E) + \alpha(E)} \quad (8)$$

where $j(E)$ represents the emissivity, incorporating contributions from thermal, line, and radiative recombination, $\alpha(E)$ includes free-free, bound-free, and radiative recombination opacity. **XSTAR** can directly compute both $j(E)$ and $\alpha(E)$ for a given ionizing flux, column density, and gas temperature. The scattering coefficient is given by $\alpha^c(E) = n_e \sigma_{cs}(E)$, where $\sigma_{cs}(E)$ is the energy-dependent Compton scattering cross section averaged over a relativistic Maxwellian electron distribution, and $n_e = 1.2n_H$ is the electron density.

The second term on the right-hand side in Eq. 8 represents the Compton scattering of photons by electrons in the gas. Unlike the Klein–Nishina scattering cross section used in previous reflection models (Ross & Fabian 2005), which is only valid for low-temperature electrons (see Figure 1 in García et al. 2020), our approach accounts for high-temperature gas by employing the Compton scattering cross section averaged over a relativistic Maxwellian electron distribution (Poutanen & Svensson 1996). The mathematical form of σ_{cs} can

¹³ We use ATDB 2024 in this paper

¹⁴ In a real disk irradiated by a compact corona, the symmetry between forward and backward directions is broken because the radiation is strongly anisotropic.

be found in Eq. B19 in Appendix B. J^c is the mean intensity after scattering:

$$J^c(E_i) = \frac{1}{\sigma_{cs}(E_i)} \int_{E_{\min}}^{E_{\max}} R(E_f, E_i) J(E_f) dE_f \quad (9)$$

where E_i and E_f are the photon energies before and after scattering, respectively, and J is the mean intensity before scattering. The Compton scattering redistribution function, R , satisfies the detailed balance condition relating the initial and final photon energies, E_i and E_f , respectively. This condition holds for a Maxwellian electron distribution and is consistent with the photons following a Wien distribution in thermal equilibrium (see Pomraning 1973, Chapter VIII):

$$R(E_f, E_i) = R(E_i, E_f) \exp\left(-\frac{E_f - E_i}{k_B T_e}\right) \quad (10)$$

Note that the photon phase-space factors are implicitly absorbed into the definition of R . We adopt the normalization condition given by (Poutanen & Svensson 1996; Madej et al. 2017):

$$\frac{\sigma_{cs}(E_i)}{\sigma_T} = \int_0^\infty R(E_i, E_f) dE_f \quad (11)$$

The redistribution function R governs the change in photon energy during the scattering process (see Appendix B). In addition to altering photon energies, Compton scattering also modifies photon propagation directions. At the present stage, we employ the angle-averaged redistribution function, consistent with the approaches used in `xillver` and `reflionx`. Suleimanov et al. (2012) showed that there exists a $\sim 2\%$ difference between the angle-dependent and angle-averaged redistribution functions in a pure hydrogen atmosphere (see their Figure 2). In future work, we plan to incorporate the full angular dependence of directional changes.

Previous public reflection models have employed a Gaussian-approximated redistribution function. In this work, we compare DAO with other models using both the Gaussian approximation and a more rigorous second-order exact redistribution function (see Section 3.1). We further quantify the deviations introduced by the Gaussian approximation in Section 3.2. The mathematical forms of both the second-order exact and Gaussian-approximated redistribution functions are provided in Appendix B. To facilitate flexibility, DAO includes a built-in selector that allows users to switch between the two redistribution schemes.

2.3. Boundary condition

The second-order radiative transfer equation (Eq. 7) can be reformulated as a block tridiagonal system of the

form $T \cdot j = R$. The detailed derivation of this transformation is provided in Appendix A. To solve this system efficiently, we employ the Thomas algorithm, which performs recursive forward elimination followed by back substitution.

The disk surface is irradiated by hard X-ray photons from the corona, while the disk itself emits thermal radiation. This configuration can be formulated as a two-boundary problem, making it suitable for solving the radiative transfer equation (Eq. 7). The upper boundary condition is determined by the incident radiation from an external source such as the corona. Following Auer (1967), we adopt the second-order exact boundary condition derived from a Taylor series (see Appendix A):

$$\mu \frac{u_2 - u_1}{\Delta\tau_{3/2}} = u_1 + \Delta\tau_{3/2} \frac{u_1 - S_1}{2\mu} + I_{\text{inc}}(\mu_{\text{inc}}) \quad (12)$$

where u_1 and u_2 are the mean-like intensities (Eq. 5) at the first and second layers, respectively; I_{inc} represents the incident intensity at incidence angle μ_{inc} , originating from the X-ray source near the disk. For the lower boundary, when $B_{\text{sw}} = 1$, a blackbody is assumed as the disk radiation to illuminate the bottom surface. The second-order exact boundary condition at the bottom is given by

$$\mu \frac{u_D - u_{D-1}}{\Delta\tau_{D-1/2}} = B_D^+ - u_D - \Delta\tau_{D-1/2} \frac{(u_D - S_D)}{2\mu} \quad (13)$$

where $D = ND$. When $B_{\text{sw}} = 0$, we have $B_D^+ = 0$. Equation A5, together with Eq. 12 and Eq. 13, forms a block tridiagonal system

$$T \cdot j = R \quad (14)$$

which is straightforward to solve by recursive forward elimination and back substitution.

2.4. Equilibrium and iteration

Convergence must be achieved through an iterative procedure. We begin by assuming that the initial radiation field at each depth is equal to the coronal illumination. Then, we use `XSTAR` to calculate the emissivity and opacity at each depth (excluding scattering in this step). The `XSTAR` calculations enforce thermal equilibrium, satisfying

$$H = C, \quad (15)$$

where H is the heating rate and C is the cooling rate. Once the plasma reaches thermal equilibrium under the current radiation field, we assume that it remains in this equilibrium state during the radiative-transfer calculation. In other words, the plasma temperature, emissivity, and absorption coefficients are held fixed in this stage.

The solution to the radiative transfer equation is obtained through a standard Λ -iteration scheme as follows:

1. Using the current temperature, emissivity, and absorption, we compute the source function (Eq. 8) at each Thomson optical depth τ_T .
2. We solve the second-order radiative transfer equation (Eq. 7) using the Feautrier method (see Appendix A).
3. We update the source function based on the new radiation field obtained at step 2 and use this new source function to update the radiation field.

This iteration loop stops when the source function converges:

$$\int \frac{S^n(E) - S^{n-1}(E)}{S^{n-1}(E)} dE < e_n, \quad e_n = 10^{-10} \quad (16)$$

After the radiation field converges in the radiative-transfer step, we again use this updated radiation field as the input to `XSTAR` to obtain a new plasma profile. We then solve the radiative transfer equation again. The iterative procedure continues until both the temperature and ionization profiles at each layer no longer change. When `DAO` calculates low-ionization models, photoionization is the dominant process, with $\alpha \gg \alpha^c$. In this regime, Eq. 16 converges more rapidly than in a scattering-dominated gas. In contrast, for high-ionization models, the gas is scattering-dominated, with $\alpha^c \gg \alpha$, leading to slower convergence. For example, Model 1 (Table 2) requires fewer than 50 steps per radiative transfer calculation to satisfy Eq. 16, while Model 3 (Table 2) requires nearly 100 steps.

The total runtime of `DAO` strongly depends on the physical conditions and model settings. In cases with low ionization parameters and soft illumination, the gas reaches cooler temperatures, which requires `XSTAR` to carry out more computationally intensive evaluations of radiative quantities at each optical depth. Consequently, the time per iteration of the main loop increases substantially. Our computations were performed on a server equipped with four sockets, each hosting an Intel(R) Xeon(R) CPU E7-8860 v3 processor. A typical run on a single core requires approximately 97 hours for the full set of iterations in Model 1 (Table 2), with each individual Λ -iteration taking about 30 minutes. In contrast, when the disk is illuminated by harder photons and set to a higher ionization parameter, as in Model 2 (Table 2), the total runtime decreases to 36 hours, while each Λ -iteration still requires roughly 30 minutes.

Considering that `XSTAR` is the most time-consuming component of the calculation and that we employ a

Model	N_E	N_τ	N_μ	$\log \xi$	Incident	Γ	kT_E
1	5000	200	10	1.0	<code>nthcomp</code>	2.0	60 kev
2	5000	200	10	3.0	<code>nthcomp</code>	1.4	60 kev
3	5000	200	10	3.0	<code>nthcomp</code>	2.0	60 keV

Table 2. Three different model sets for moderate `nthcomp` incident with low ionization degree gas (Model 1), hard `nthcomp` incident with high ionization degree gas (Model 2) and moderate `nthcomp` incident with high ionization degree gas (Model 3)

high energy resolution, we do not use the Accelerated Lambda Iteration (ALI) method in this work. In our case, the accelerated Λ^* -operator becomes a full matrix of dimension $N_{\tau_T} \times N_E \times N_E$ because the partial redistribution function (specifically, the scattering redistribution function in our context) is considered (Paletou & Auer 1995), making the corresponding linear system prohibitively expensive to solve. Moreover, Suleimanov et al. (2012) demonstrated that ALI still requires a large number of iterations when the exact Compton scattering redistribution function is used.

3. RESULTS

3.1. Comparison with Other Models

First, we employ the `nthcomp` model (Zdziarski et al. 1996; Źycki et al. 1999) as the illuminating source at the top boundary. We set $I_{\text{type}} = \text{file}$ and obtain the incident spectrum by setting the reflection fraction to 0, $\Gamma = 2.0$, and $kT_E = 60$ keV in `xillvercp`; this spectrum is then adopted as the standard incident radiation field in this paper. The results are compared with the `reflionx_hd_nthcomp` (Ross & Fabian 2007; Jiang et al. 2020) and `xillvercp` tables. To match these models, we do not adopt any bottom incident radiation field; thus, we set $B_{\text{sw}} = 0$. Our model and `xillvercp` adopt the solar abundances table from Grevesse et al. (1996) for elements from H to Zn, in contrast to the `reflionx` model, which uses the abundances from Morrison & McCammon (1983). Accordingly, in this section, we set A_{Fe} in our model and `xillvercp` to 1.32 to match the setting in `reflionx`. In addition, we set $\log \xi = 1.0$ (top row), 2.0 (middle row), and 3.0 (bottom row), and adopt both the Gaussian approximation (left column) and the exact energy redistribution function (right column) for Compton scattering in Figure 1. All other parameters are set to their default values listed in Table 1.

The spectra in Figure 1 are plotted in the form of EJ_E . The `reflionx` model assumes an isotropic radiation field, whereas both `DAO` and `xillver` compute an anisotropic radiation field. For `DAO` and `xillver`, the mean intensity is evaluated as $J(E) = \int I(\mu, E) d\mu$,

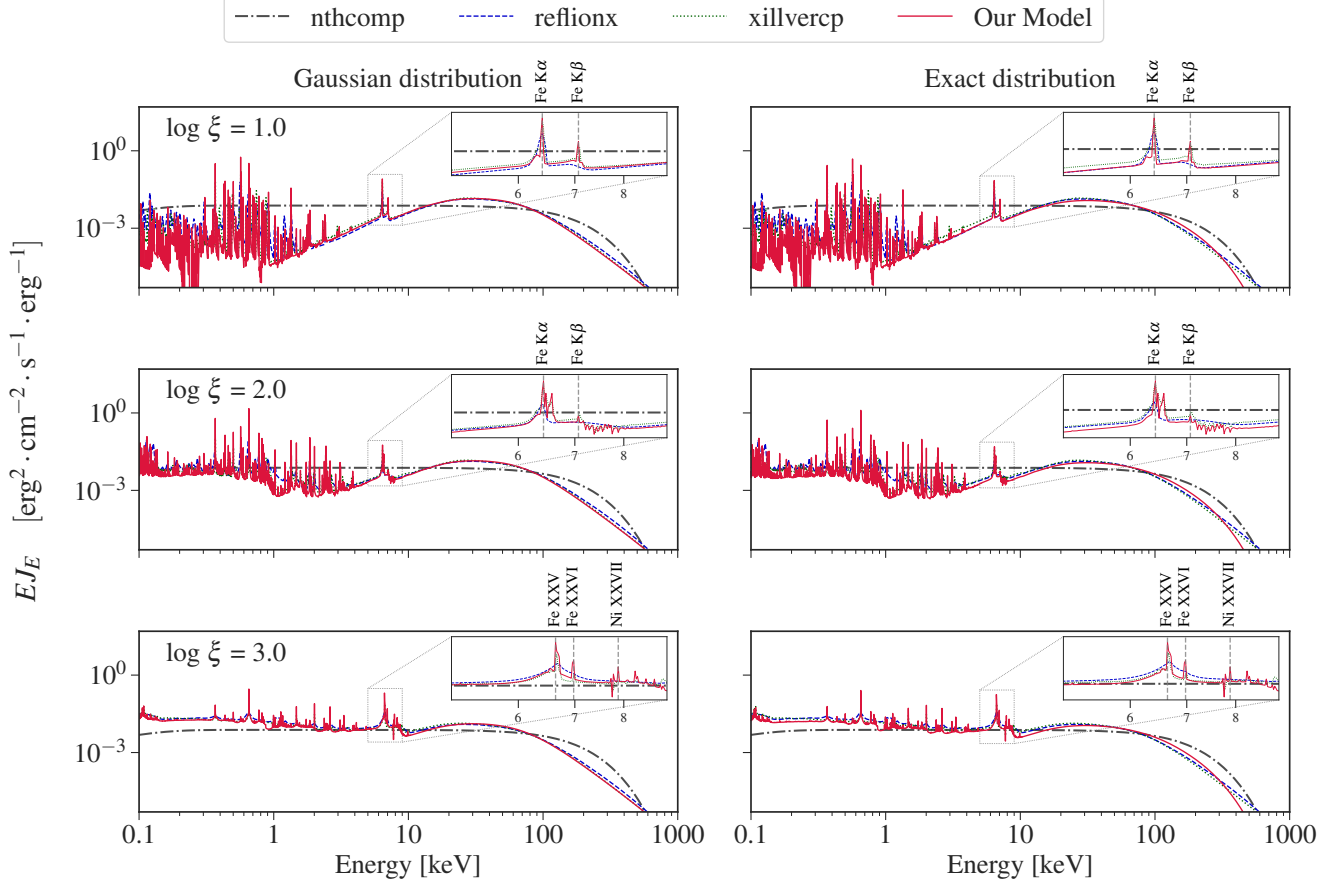


Figure 1. Reflection spectra generated by our model (DAO, red solid line), compared with those from `reflionx` (blue dashed line) and `xillvercp` (green dotted line). The incident `nthcomp` spectrum from `xillvercp` (`refl_frac=0, Γ = 2, kT_E = 60 keV`) is depicted by the grey dash-dotted line, iron abundance is set at 1.32 for DAO and `xillver` to account for different abundance tables. Other parameters are set at default their value as shown in Table 1. To compare fairly with `reflionx` and `xillver`, we also run DAO using the Gaussian approximation. Left column: Gaussian-approximated redistribution function. Right column: exact redistribution function. All spectra are normalized by their integral of energy, $EJ_{\text{norm}}(E) = EJ(E) / \int EJ(E) dE$.

where $μ$ is sampled according to the internal angular discretization adopted in each model¹⁵. As illustrated in Figure 1, the outputs of the three models are consistent within the 0.1 to 1000 keV range. All three models exhibit a prominent Compton hump, strong absorption edges and emission lines. In particular, in the spectrum generated using the exact redistribution, the Compton hump drops more rapidly at higher energies. In Section 3.2, we analyze in detail the impact of different redistribution functions.

In the low-ionization atmosphere ($\log \xi = 1.0$), we observe both the iron $K\alpha$ line and the $K\beta$ line in DAO and `xillvercp`. The intensities of the iron lines in DAO are

very close to those in `xillvercp` in this case. However, due to limitations in its atomic database, `reflionx` does not include any iron $K\beta$ transitions. For the intermediate-ionization atmosphere ($\log \xi = 2.0$), the $Fe\ K\alpha$ emission profile resolves into a complex structure comprising three discrete features in both DAO and `xillvercp`: a dominant peak at 6.43 keV (corresponding to low-ionization $Fe_{\text{VII-XVII}}$), a secondary component near 6.51 keV (attributable to intermediate L-shell ions, $Fe_{\text{XVIII-XX}}$), and a distinct high-energy peak at 6.58 keV (consistent with $Fe_{\text{XXI-XXII}}$). This profile reveals that the plasma at $\log \xi = 2.0$ comprises a rich mixture of various iron ionization states. For the highly ionized atmosphere ($\log \xi = 3.0$), we observe the Fe_{XXV} and Fe_{XXVI} $K\alpha$ lines, as well as a high-energy feature around 7.9 keV. This latter feature is identified as a blend of the Ni_{XXVII} $K\alpha$ line and the Fe_{XXV} $K\beta$ transition. Figure

¹⁵ If we choose $N_\mu = 10$, our angle grid is the same as `xillver`'s: $μ = \{0.05, 0.15, 0.25, 0.35, 0.45, 0.55, 0.65, 0.75, 0.85, 0.95\}$.

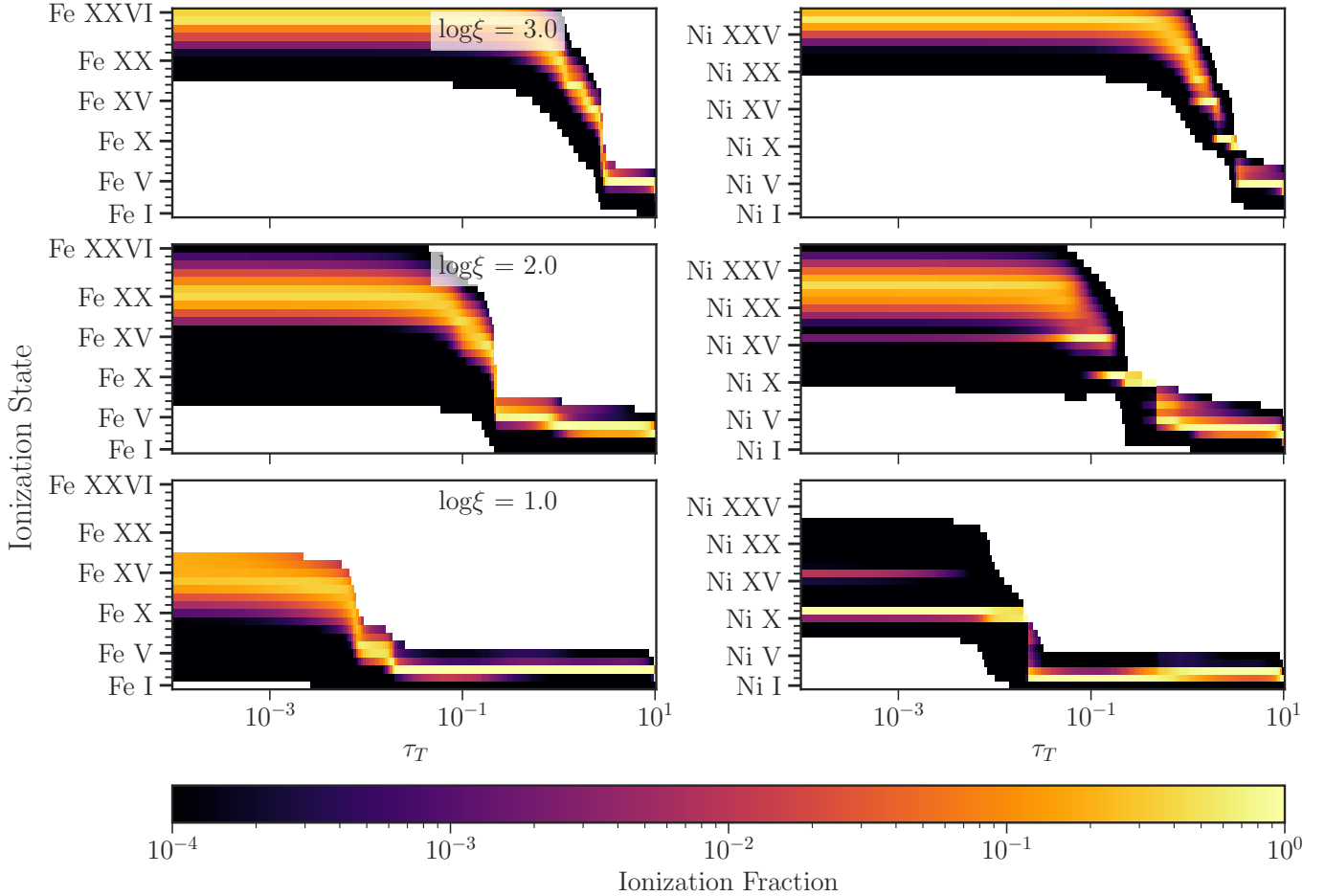


Figure 2. Ions fraction of Fe and Ni for reflection shown in Figure 1

2 reveals a significant coexistence of helium-like Fe and Ni ions within the highly ionized atmosphere. Regarding the absence of Nickel features at lower ionization states: The high-energy feature observed at $\log \xi = 3.0$ cannot be observed in intermediate- or low-ionization atmospheres. In these cases, the Nickel line energy consistently falls above the Iron K-edge energy. Since Nickel is much less abundant than Iron ($\sim 1/17$), the strong absorption from Iron suppresses the Nickel emission, making the line invisible. In contrast, this $\text{Ni}_{\text{XXVII}} \text{K}\alpha$ feature is absent in the `xillvercp` and `reflionx` table models, as these models do not include atomic calculations for Nickel.

The detectability of Nickel in astrophysical spectra is well-supported by observations. Narrow $\text{Ni K}\alpha$ emission lines have been robustly detected in the X-ray spectra of bright AGNs (Molendi et al. 2003). In the regime of High-Mass X-ray Binaries, detailed spectroscopy of GX 301-2 using Suzaku (Suchy et al. 2012) has explicitly resolved the $\text{Ni K}\alpha$ line at ≈ 7.47 keV, separating it from the dominant iron complex. Consequently, in highly ionized environments where the Fe K-edge absorption is di-

minished, the $\text{Ni K}\alpha$ line predicted by our model should be observable, particularly with the high-resolution capabilities of future missions like *NewAthena*.

We also test our model with a softer and a harder illumination, specifically $\Gamma = 1.4$ and $\Gamma = 2.4$, with the results presented in Figure 3. In Figure 3, the ionization parameter is set at 3.0 for all spectra; the other parameters are the same as in Figure 1. Hard X-ray illumination with exact scattering redistribution displays a notable difference in the Compton hump from that of the Gaussian-approximated redistribution. This is caused by the inaccuracy of the Gaussian-approximation redistribution function for high-energy photons and electrons (see Section 3.2 for more details). However, we also find noticeable discrepancies among the three models in the soft X-ray band (0.1–1 keV) for any `nthcomp` incident spectrum. Light-element α lines (e.g., C, N, O) as well as Fe L-shell emission lines are generally present in this energy range. For `reflionx`, such discrepancies are expected because the model includes only a limited set of ions. In contrast, the differences in the soft X-ray range between `xillver` and `DAO` most likely arise from

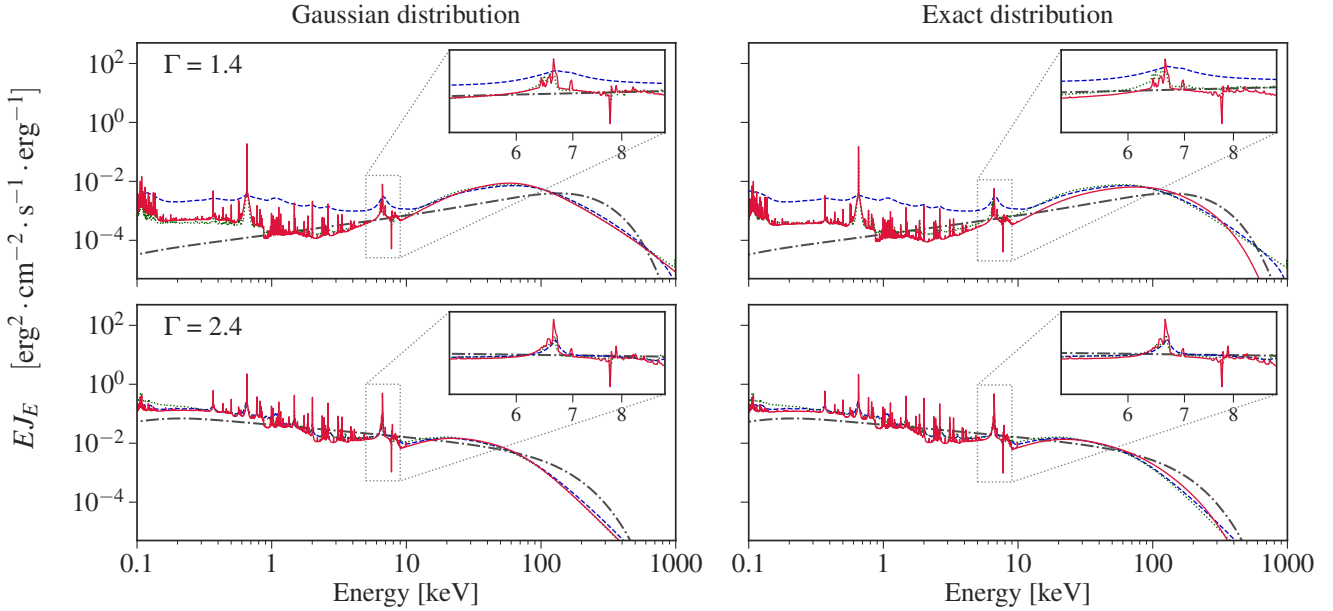


Figure 3. Same as Figure 1, but with different `nthcomp` incident spectra obtained from `xillvercp` by setting `refl_frac = 0`, $kT_e = 60$ keV, and $\Gamma = 1.4$ (top panel) and $\Gamma = 2.4$ (bottom panel). The ionization parameter is set to $\log \xi = 3.0$ for all spectra.

Model	Atomic data table	XSTAR version
DAO	ATDB (2024-10-17T14:09:13) (Mendoza et al. 2021)	2.59 (Kallman et al. 2021)
xillvercp	ATDB (2012-08-03T01:58:54)	2.2.1bn (Kallman & Bautista 2001)
reflionx	custom definition (see Ross & Fabian 2005)	not used

Table 3. Atomic physics treatments in the three models

the use of different atomic databases and different versions of XSTAR in their calculations. Table 3 summarizes the XSTAR versions and atomic data tables employed by each code. The ATDB 2024 release incorporates corrections for high-density plasma effects and improved radiative and collisional rates for odd- Z elements, with related developments reported in Mendoza et al. (2017, 2018, 2021). Moreover, Ding et al. (2024) demonstrated the impact of the latest XSTAR and ATDB versions on reflection spectra, as shown in their Figures 3 and 4. They also found that using different versions of XSTAR and atomic databases in the `xillver` model produced noticeable differences.

In summary, DAO provides a more accurate treatment of atomic processes by employing the latest versions of XSTAR and ATDB, and it achieves a more precise description of Compton scattering through the use of the exact redistribution function. Furthermore, we compare DAO with `pexrav` (Magdziarz & Zdziarski 1995) to validate our treatment of Compton scattering. The results are shown in Figure 17 in Appendix A. Although the `pexrav`

spectrum exhibits a slightly higher peak in the Compton hump, the two models are consistent at energies $E < 20$ keV and $E > 50$ keV.

3.2. Effects of Energy Redistribution Functions

Compton scattering is a stochastic process that alters both the propagation direction and the energy of photons, and it should be described using the exact quantum mechanical formalism. However, models such as `xillver` and `reflionx` adopt a Gaussian approximation (Ross et al. 1978) to treat this process, which is only valid to describe the energy redistribution for low-energy photons ($E_{\text{ph}} \ll m_e c^2$) scattered by low-temperature electron clouds ($kT_e \ll E_{\text{ph}}$). Appendix Figure 18 illustrates the differences between the exact and Gaussian redistribution functions. (1) At low electron temperatures and for soft incident photons ($E_i = 1$ keV), both the Gaussian and exact redistribution functions exhibit a single peak with good symmetry. (2) When the incident photon energy approaches $m_e c^2$ while the electron temperature remains low, the exact redistribu-

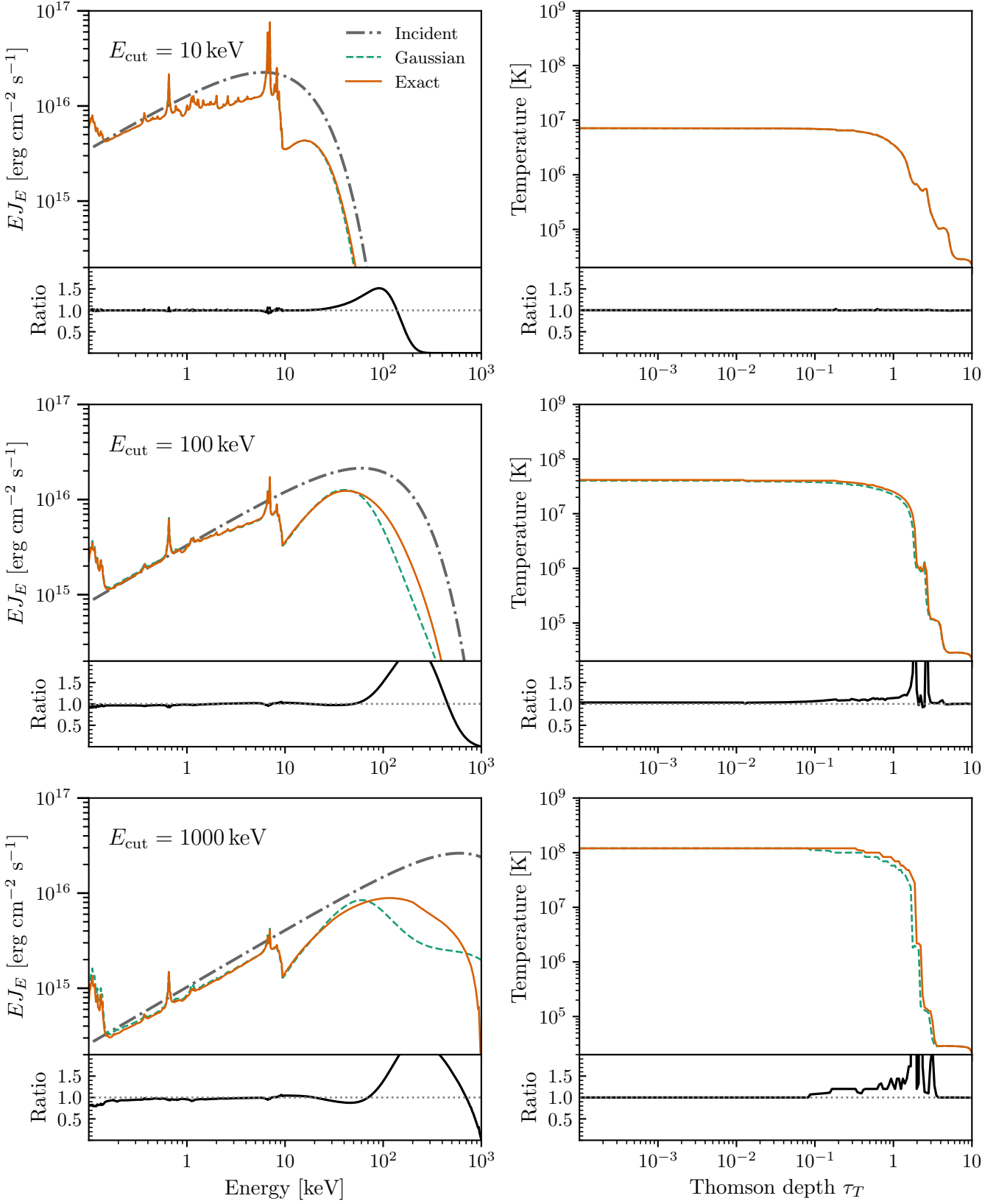


Figure 4. Comparison of angle-averaged reflection spectra computed using the exact (red solid line) and Gaussian (green dashed line) redistribution functions. The incident cut-off power-law spectrum is shown as a grey dashed line. The parameters are $\Gamma = 1.4$, $A_{\text{Fe}} = 5.0$, and $\log \xi = 3.5$, with varying cut-off energies of $E_{\text{cut}} = 10$ keV (top), 100 keV (middle), and 1000 keV (bottom). Other parameters are set at their default value. The lower sub-panel in each plot displays the ratio of the spectrum computed with the exact redistribution to that computed with the Gaussian approximation.

tion function develops a double-peaked and asymmetric structure. (3) At sufficiently high electron temperatures (e.g., $T = 10^9$ K), the Gaussian approximation becomes excessively broadened and no longer captures the actual shape of the Compton scattering redistribution. García et al. (2020) investigated this effect on the reflection spectrum, but it has not been implemented in a publicly released table model before.

The exact redistribution function for Compton scattering has been extensively studied. Guilbert (1981) incorporated the relativistic Maxwellian velocity distribution into the redistribution function, but a computational error was present in the original paper. Subsequently, Nagirner & Poutanen (1993), Poutanen & Svensson (1996), and Poutanen & Vurm (2010) investigated the redistribution function for photons scattered by anisotropic electrons using quantum electrodynamical methods. Later, Madej et al. (2017) corrected the earlier error in Guilbert (1981) and demonstrated consistency among these methods. García et al. (2020) used the method described in Nagirner & Poutanen (1993) and showed reflection spectra using the exact redistribution function. We present the algorithms for the Gaussian-approximated and quantum-mechanical redistribution functions in Appendix B.

Figures 1–3 display that a discrepancy exists between the reflection spectra generated by the exact redistribution and those from the Gaussian approximation within the hard X-ray band. In Figure 4, we investigate this further by considering a cut-off power-law as the incident spectrum with $\Gamma = 1.4$ and a variety of cut-off energies ($E_c = 10, 100, 1000$ keV). To show how this could impact the Compton shoulder of K α lines at 6.4 keV and Compton hump, we set the iron abundance to 5.0 and ionization parameter at 3.5. Other parameters are set at default values. The angle-averaged spectra shown in the left column and the temperature profiles in the right column clearly illustrate how these differences depend on temperature. The surface temperature is highest for the hardest incident spectrum ($E_c = 1000$ keV), and in this case the differences in the reflection spectrum between the two methods are most pronounced. However, for the coolest gas, where the surface temperature is an order of magnitude lower than in the former case, the impact of the inaccurate Gaussian redistribution function is smaller, but can still be observed in the ratio plot. Compared with the large difference in the Compton hump region, the deviation of the Compton shoulder is not very obvious for all three models.

Current instruments, such as *NuSTAR*, can image the sky in the 3–79 keV band, while *Insight-HXMT* extends observations to hard X-ray energies up to 250 keV

(Zhang et al. 2020). Both of them can observe the hard X-ray band, where deviations in measurements arise, especially for hard spectra and high coronal temperatures (Kara et al. 2017; Buisson et al. 2019). We therefore employ the exact redistribution function for all subsequent calculations.

3.3. Effects of varying the ionization parameter

We assume a constant-density atmosphere, and the form of Tarter et al. (1969) is used to calculate the ionization parameter ξ (Eq. 2). At each optical depth layer, the total ionizing flux F_x of the radiation field is calculated to obtain the ionization parameter. Figure 5 illustrates the emergent spectra for various ionization parameters, considering the exact redistribution function for Compton scattering. No normalization has been applied to the final spectra displayed in this plot. It is evident that spectra corresponding to a higher ionization parameter exhibit greater luminosity, whereas spectra with a lower ionization parameter display more prominent atomic line features and the Compton shoulder.

Figure 6 shows the temperature profile as a function of the Thomson optical depth (from 10^{-4} to 10) for the two incident spectra shown in Figure 5. In a highly ionized atmosphere, the dominant heating process is electron recoil following Compton scattering. The net heating rate is given by Ross et al. (1978)

$$n_e \Gamma_e = \frac{\sigma_T}{m_e c^2} \left(\int_0^\infty E J_E dE - 4kT \int J_E dE \right) \quad (17)$$

where Γ_e is the net Compton heating rate, n_e is the electron density, E is the energy, J_E is the mean intensity, σ_T is the Thomson cross section, $m_e c^2$ is the electron rest energy, k is the Boltzmann constant, and T is the electron temperature. The Compton heating rate is related to $E J_E$, which implies a large heating rate when there are more photons in the hard X-ray band. In a less ionized atmosphere, the dominant heating process is photoionization, which is sensitive to the soft X-ray band. Consequently, the surface temperature for the lowest ionization parameter ($\log \xi = 1.0$) under a soft X-ray incident spectrum is higher than that under a hard X-ray incident spectrum. Conversely, the surface temperature for the highest ionization parameter ($\log \xi = 4.0$) under a hard X-ray incident spectrum is higher than that under a soft X-ray incident spectrum because of Compton heating.

In summary, the ionization parameter affects how photons interact with electrons and ions in the gas. Such effects change the temperature profile and the spectral shape. In Figure 7, we show the reflection spectra (left), the ionization parameter (middle), and the temperature

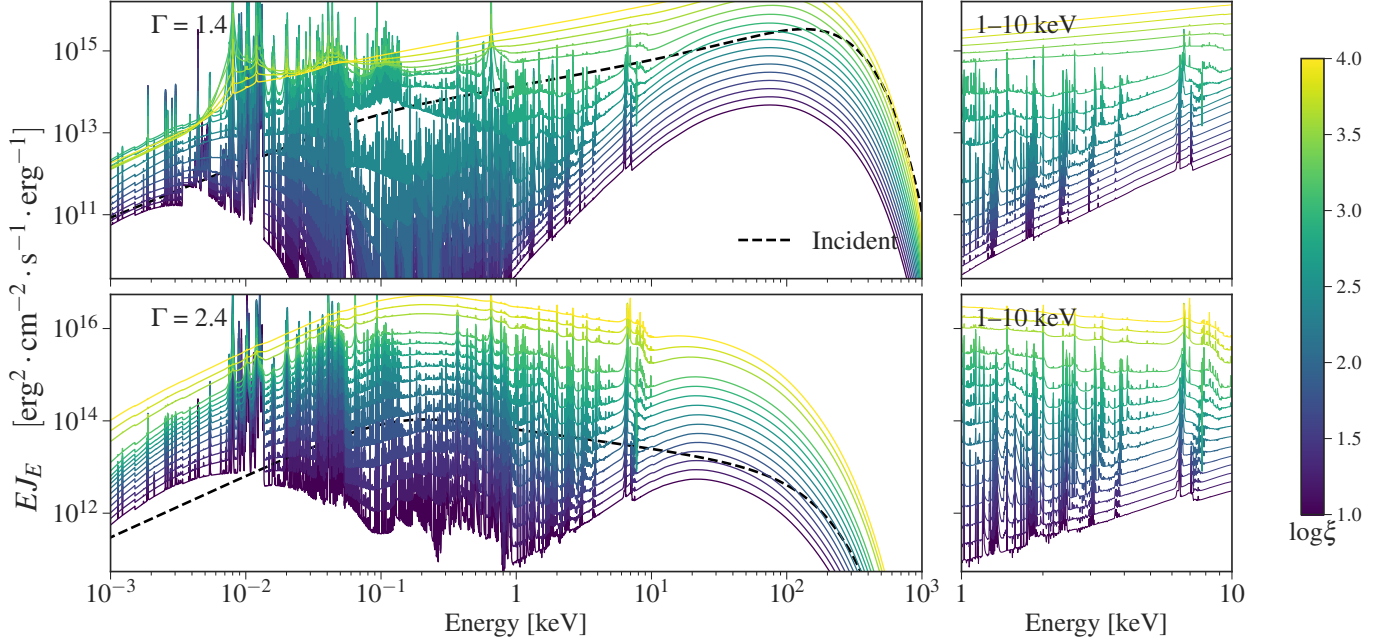


Figure 5. Angle-averaged reflection spectra for various ionization parameters ($\log \xi$), distinguished by color. The `nthcomp` incident spectra are obtained from `xillvercp` by setting `refl_frac` = 0 and kT_E = 60 keV, with Γ = 1.4 (top panel) and Γ = 2.4 (bottom panel). Other parameters are set at their default values. The shape of incident spectrum is shown as a black dashed line for comparison.

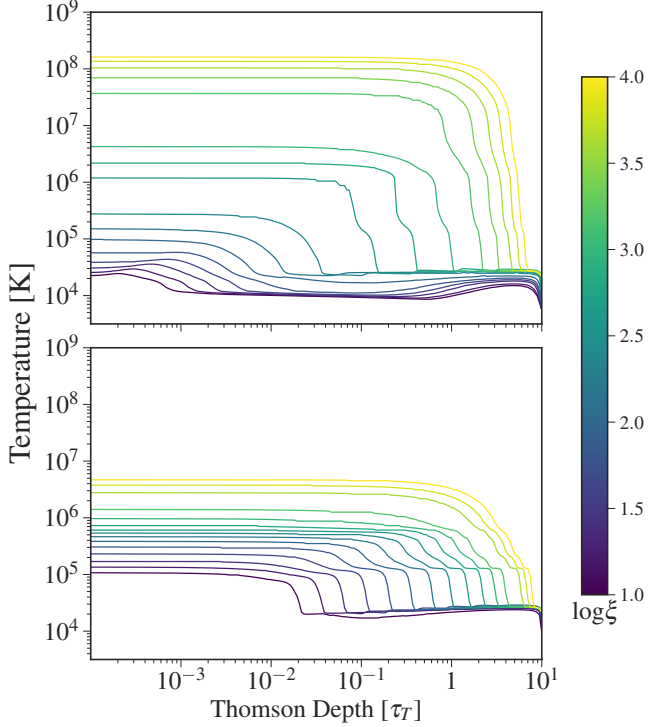


Figure 6. Gas temperature for different ionization parameters, parameters set as same as Figure 5.

profile (right) as a function of optical depth in the final iteration step. Corresponding ionic fractions for iron (Fe), oxygen (O), and carbon (C) are visualized as col-

ormaps in Figure 8. The incident spectrum for these plots is a Comptonization spectrum with Γ = 2.0 as shown in the first panel of Figure 7.

Figure 8 shows that multiple intermediate and highly ionized states of Fe, C, and O appear in the upper layers ($\tau_T < 0.1$) of a weakly ionized disk ($\log \xi = 2.0$). As the depth increases, these ions gradually transition to lower ionization states due to the decrease in the ionizing flux. The high abundance of these ions in the upper layers leads to strong K-, L-, and M-shell transition lines in the emergent reflection spectra (see Figure 7). In contrast, at the highest ionization parameter ($\log \xi = 4.0$), the ionization balance shifts strongly toward more highly stripped ions, driving the transition zones of each element to greater depths within the slab. For example, in such a highly ionized disk, only H-like and He-like species such as Fe xxvi and Fe xxv persist (Figure 8, top row). As a result, the $K\alpha$ line at 6.4 keV from neutral or low-ionization iron is entirely absent in the reflection spectrum (Figure 7, bright green line). Furthermore, the equivalent widths of the remaining $K\alpha$ lines from Fe xxvi (~ 6.97 keV) and Fe xxv (~ 6.7 keV) are significantly diminished by the strong Compton scattering continuum (see Figure 9 for details). In contrast, for the lower ionization cases of $\log \xi = 2.0$ and 3.0, the 1–10 keV band exhibits a much richer emission-line spectrum. This energy range is populated not only by the complex iron $K\alpha$ and $K\beta$ transition series but also

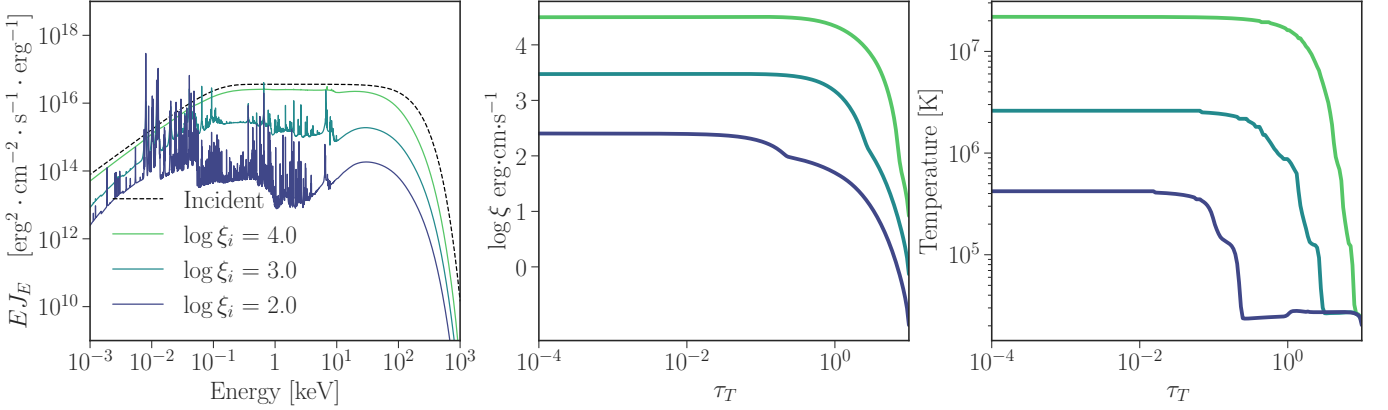


Figure 7. Left: Angle-averaged reflection spectra for different ionization parameters ($\log \xi_i$). The incident radiation is a Comptonization spectrum with $\Gamma = 2.0$. The incident spectrum for the $\log \xi_i = 4.0$ case is plotted in the left panel for reference. Middle and Right: Profiles of the ionization parameter (Middle) and gas temperature (Right) as a function of optical depth.

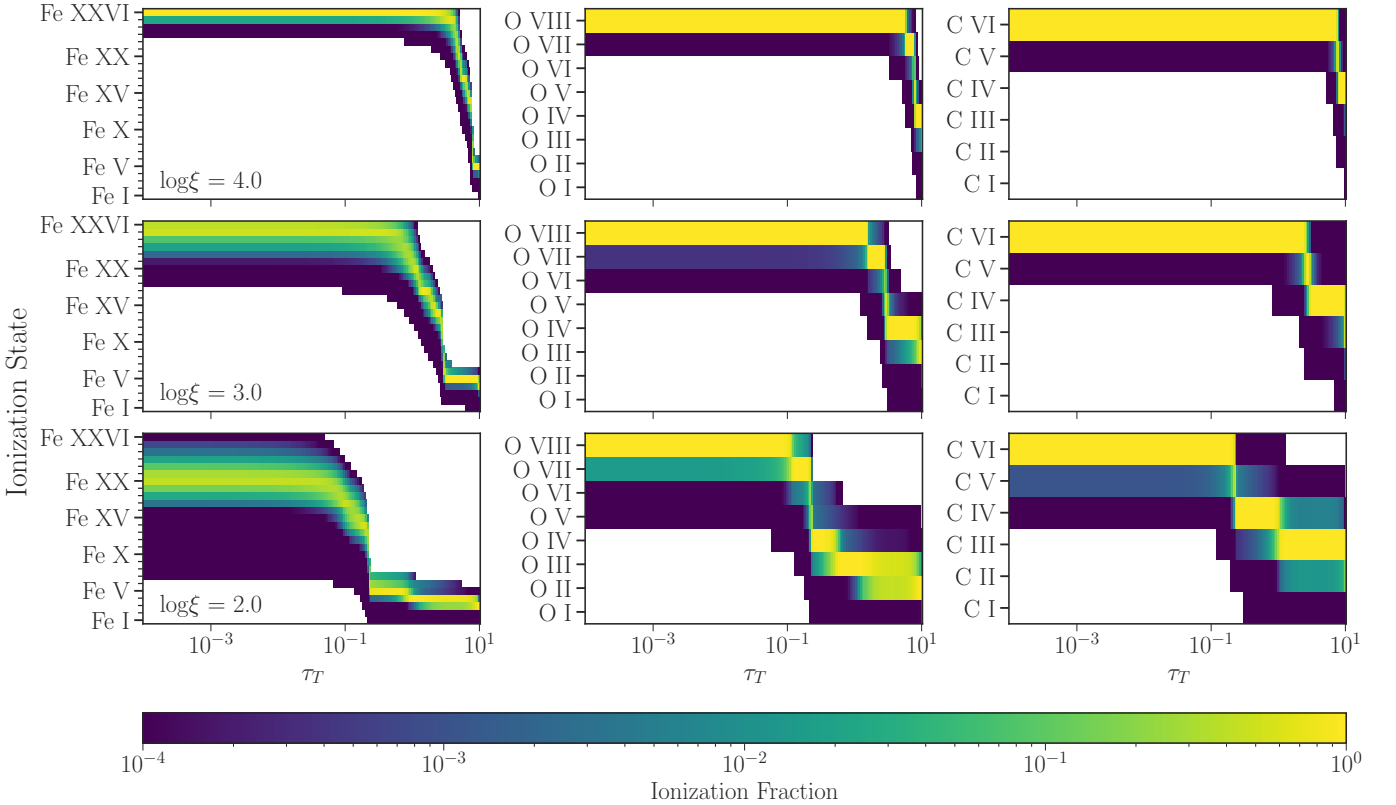


Figure 8. Ionic fractions of iron (Fe), oxygen (O), and carbon (C) as a function of Thomson optical depth for three different ionization parameters: $\log \xi = 4.0$ (top row), $\log \xi = 3.0$ (middle row), and $\log \xi = 2.0$ (bottom row). The other parameters are the same as in Figure 7.

by K-shell transitions from lighter elements (e.g., S, Ar, Ca) as a wider range of ionization states contribute.

3.4. Effects of varying the incident angle

In our model, the coronal illumination field is specified by a single incidence angle. The I_{inc} at the top boundary of the second-order radiative transfer equation (Eq. 12) is set to zero everywhere except at μ_{inc} . Since the flux

is defined as the first moment of the intensity,

$$F_x(\tau, E) = \int_0^1 u(\tau, E, \mu) \mu d\mu, \quad (18)$$

where $\mu = \cos \theta$, and we adopt

$$I = I_{\text{inc}} \delta(\mu - \mu_{\text{inc}}). \quad (19)$$

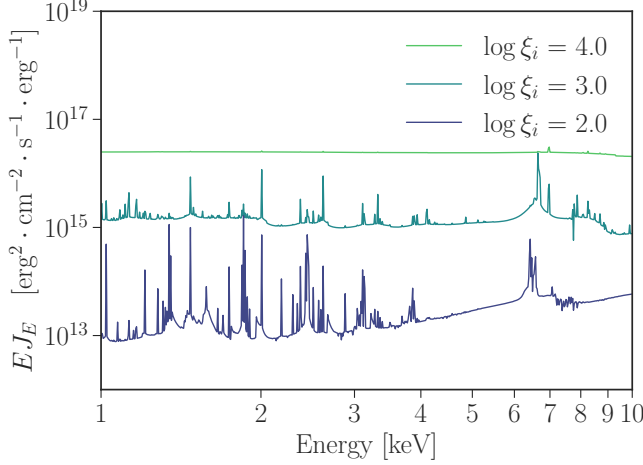


Figure 9. Evolution of the reflection spectrum in the 1–10 keV band as a function of the ionization parameter ξ . The color gradient represents the transition from low ionization (dark blue, $\log \xi = 2.0$) to a nearly fully ionized plasma (bright green, $\log \xi = 4.0$). The lower ionization models exhibit a rich spectrum of K α and K β emission lines, whereas these features are significantly diminished by the strong Compton scattering continuum in the highest ionization case.

The incident intensity at the top boundary can then be evaluated as

$$I_{\text{inc}}(E) = \frac{2F_x(E)}{\mu_{\text{inc}}}. \quad (20)$$

In DAO, we always calculate $F_x(E)$ first and then use Eq. 20 to derive I_{inc} for the boundary condition (Eq. 12). This relation shows that the incidence angle μ_{inc} directly affects the illumination intensity, which in turn influences the radiative transfer solution. Consequently, a smaller μ_{inc} is expected to produce higher gas temperatures and a higher degree of ionization at the surface.

Figure 10 shows the emission-angle-averaged flux for different incidence angles. Incidence angles are sampled from 0.1 to 0.9 in steps of 0.1 (color-coded from purple to yellow). The illumination radiation field is modeled with a cut-off power-law, using $\Gamma = 2.0$ and $E_{\text{cut}} = 300$ keV. The ionization parameter is set to 2.0, and the number of angular grids is fixed at $N_\mu = 30$ to improve the angular resolution, while all other model parameters are set to their default values. The results are broadly consistent with our expectation: the gas temperature and the strength of the radiation hump show a clear inverse correlation with $\cos \theta_{\text{inc}}$.

On the other hand, the incidence angle directly affects the radiative transfer solution. To focus on this effect, we consider a purely scattering atmosphere with a fixed gas temperature of 10^9 K, thereby suppressing variations in ionization and temperature profile that would otherwise arise from changes in the effective radiation in-

tensity. This setup allows us to focus solely on the role of the incidence angle. In this case, the source function can be expressed as

$$S(E) = \frac{1}{2\sigma(E)} \int dE' R(E', E) \int_{-1}^1 d\mu I(E', \mu) \quad (21)$$

which is the second term in Eq. 8 with $\alpha(E) = 0$.

Figure 11 displays the angle-averaged emergent spectra. After a few iterations, all spectra reveal a prominent Compton scattering hump at high energies. This hump is weakest for the most grazing incidence angle ($\mu_{\text{inc}} = 0.1$), despite this case having the strongest effective incident radiation (Eq. 20). This behavior is consistent with the reflection spectra in Figure 10, where the intensity of the Compton hump relative to the iron line is significantly greater at small μ_{inc} than at large ones.

In summary, the incidence angle fundamentally influences the reflection spectrum through two distinct mechanisms: 1) it determines the effective radiation intensity incident on the disk, thereby governing the ionization balance and temperature profile, and 2) it is an explicit parameter in the angular dependence of the radiative transfer equation. While the `xillver` table model neglects the latter, our approach explicitly incorporates this dependence. Notwithstanding this advancement, a key approximation remains in our model: the source function does not yet account for the angular distribution of scattering. The effects of this simplification on data analysis are deferred to a future publication.

3.5. Emergent intensity along all angle bins

Depending on the choice of angular binning, the emergent intensity can be obtained for different emission angles. In the special case where $\mu_{\text{inc}} = \mu_{\text{emis}}$, the emergent radiation field is given by

$$I^+(\mu_{\text{emis}}) = 2u(\mu_{\text{emis}}) - I^- \quad (22)$$

where I^- denotes the illuminating spectrum from the corona. At other emission angles, the emergent radiation field is given by

$$I_{\mu_{\text{emis}}}^+ = 2u_{\mu_{\text{emis}}} \quad (23)$$

As shown in Figure 12, the radiation intensity decreases as μ increases. This behavior is primarily driven by the effective optical depth, defined as

$$\tau_{\text{eff}} = \frac{\tau}{\mu} \quad (24)$$

Photons escaping at grazing angles (low μ) traverse a longer effective path through the medium. Consequently, spectral features originating from deeper layers, such as emission lines from heavy elements (e.g.,

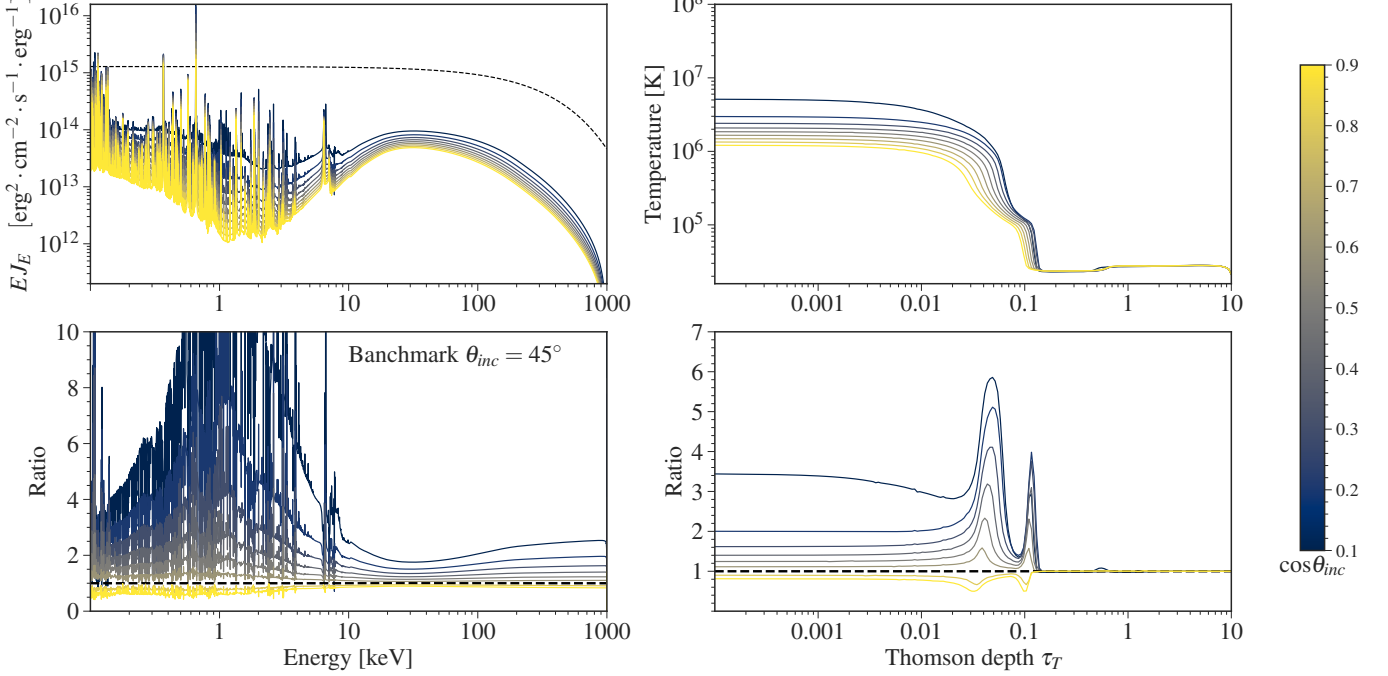


Figure 10. Top row: Angle-averaged emergent intensity (left) and the corresponding temperature profiles (right), color-coded by the incidence angle $\cos \theta_{\text{inc}}$. Bottom row: Spectral ratios relative to the $\theta_{\text{inc}} = 45^\circ$ case for all incidence angles. The incidence angles are sampled linearly in $\mu = \cos \theta_{\text{inc}}$ between 0 and 1 using 30 bins. The ionization parameter is $\log \xi = 2.0$, and the incident radiation field (black dashed line) is a cut-off power-law with $\Gamma = 2.0$ and $E_{\text{cut}} = 300$ keV. The other parameters are set at their default values.

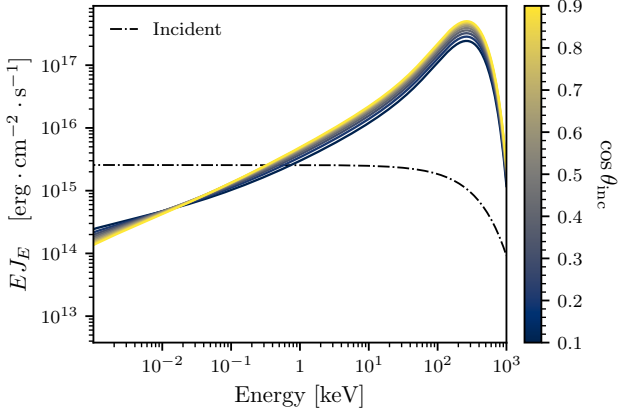


Figure 11. Solution of the radiative transfer equation for a pure scattering atmosphere. The incident spectrum is a cut-off power-law ($\Gamma = 2.0$, $E_{\text{cut}} = 300$ keV), and the gas temperature is fixed at 10^9 K.

Fe), suffer stronger attenuation compared to those produced near the surface (e.g., C, O). For hard X-ray photons, the extended path length increases the probability of scattering, rendering the Compton hump highly sensitive to minor variations in optical depth. This effect, well established in previous works (Lightman et al. 1981; Lightman & White 1988; Magdziarz & Zdziarski 1995), is critical for interpreting the continuum. Indeed, Figure

12 reveals that the Compton hump is most pronounced at the smallest cosine of the emergent angle.

The angular dependence of the emissivity plays a vital role in determining the observed spectrum (e.g., Liu et al. 2025). Recently, Huang et al. (2025) highlighted the impact of emission angles on relativistic spectra shaped by strong gravity. In Appendix C, we present relativistic spectra calculated using the formalism adopted from the `relconv`, `relxill` and `relxillA` model.

3.6. Effects of varying the hydrogen density

Currently, DAO assumes reflection in a constant-density slab, with a default hydrogen density of 10^{15} cm^{-3} . In AGN or XRB systems, the disk densities are sometimes greater than 10^{15} cm^{-3} (Jiang et al. 2019) and sometimes even higher than 10^{20} cm^{-3} (Liu et al. 2023a). However, the standard XSTAR atomic table (ADTB) only supports hydrogen densities lower than 10^{18} cm^{-3} ; a specific atomic database is needed for higher hydrogen densities (Kallman et al. 2021). DAO will be updated to consider higher densities once the atomic database is available.

In Figure 13, we compare reflection spectra for hydrogen densities of 10^{15} , 10^{16} , and 10^{17} cm^{-3} under `nthcomp` illumination. Other parameters are set at their default values. The results are consistent with the findings of García et al. (2016): for a given ionization pa-

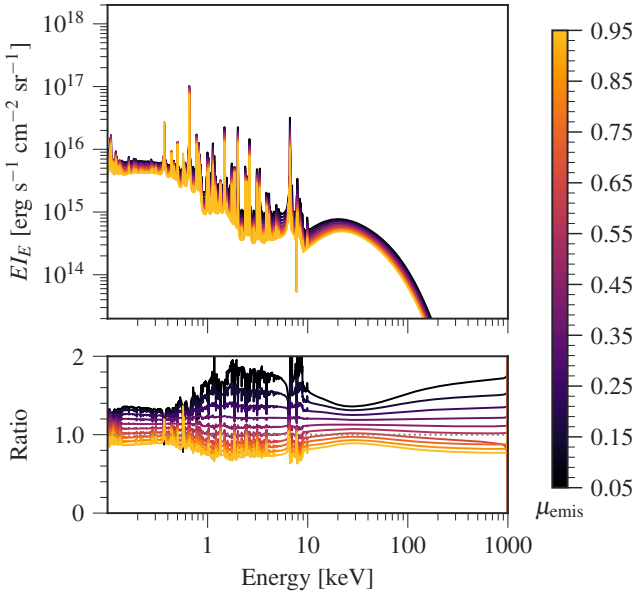


Figure 12. Emergent intensity spectra (top panel) and the ratio of emergent intensity to the angle-averaged intensity (bottom panel) for a fixed incident angle of $\theta_{\text{inc}} = 45^\circ$. The profiles are color-coded by the cosine of the emission angle, μ_{emis} .

parameter, the gas temperature increases with hydrogen density, and the continuum emission in the low energy band displays clear differences among these spectra.

To further study the density effects in the soft X-ray band and temperature profile, we perform additional calculations with a blackbody incident spectrum of temperature 1 keV, which allows us to focus on the soft X-ray band. As shown in Figure 14, the Compton hump is weaker under this type of illumination than for a power-law incident spectrum, and the high-energy parts of the spectra become nearly identical across different densities. However, noticeable differences persist in the low-energy continuum emission. The temperature profiles show obvious differences at large optical depths.

The n_h^2 dependence of bremsstrahlung heating and cooling rates plays an important role in shaping the temperature profile of the reflection region. The bremsstrahlung heating rate is related to the free-free absorption coefficient through

$$H_{\text{ff}} = \int \alpha_{\text{ff}}(E) j(E) dE, \quad (25)$$

where the free-free absorption coefficient α_{ff} is

$$\alpha_{\nu}^{\text{ff}} = 3.7 \times 10^8 Z^2 n_e n_z \bar{g}_{\text{ff}} T^{-1/2} \nu^{-3} \left(1 - e^{-h\nu/kT}\right). \quad (26)$$

Here, n_e is the electron density, n_z is the density of that ion, $\bar{g}_{\text{ff}}(T, \nu)$ is the velocity-averaged Gaunt factor, T is

the electron temperature, Z is the charge of the most abundant ion, and the bremsstrahlung emissivity j is given by

$$j_{\nu} = 6.8 \times 10^{-38} Z^2 n_e n_z T^{-1/2} e^{-h\nu/kT} \bar{g}_{\text{ff}}. \quad (27)$$

The bremsstrahlung cooling rate can be expressed as

$$\Gamma_{\text{ff}} = 1.42 \times 10^{-27} T^{1/2} Z^2 n_e n_z \bar{g}_{\text{ff}}. \quad (28)$$

It is evident from the above expressions that both the heating and cooling rates scale as n_h^2 , so even modest increases in density can dramatically alter the thermal balance of the gas. By contrast, the net Compton heating-cooling rate in the non-relativistic limit is given by Eq. 17, which mainly depends on photons' energies. Thus, while Compton processes dominate in the hard X-ray band, bremsstrahlung heating and cooling become increasingly important in the high-density regime due to their quadratic dependence on n_h .

Figures 15–16 show the heating and cooling rates associated with the spectra in Figure 14. These rates govern the gas temperature at each layer and ultimately shape the emergent spectrum. As seen in Figure 15, bremsstrahlung heating and cooling vary strongly in the deeper layers. By contrast, Compton heating remains nearly independent of hydrogen density in these regions, and Compton cooling exhibits only minor variations compared with bremsstrahlung cooling. A larger discrepancy is expected for $\log(n_h) > 18$, a regime that will be investigated in future work.

4. DISCUSSION

In this paper, we presented a new reflection model, which we named **DAO**. This model is open-source and highly flexible for studying the reflection phenomenon in accretion-disk-corona systems. The model assumes a slab geometry, with the parameters of the slab and the incident radiation field listed in Table 1. It uses the **XSTAR** code to calculate the photoionization of each layer and the Feautrier method to solve the radiative transfer through the layers.

We compared our new X-ray reflection model **DAO** with **xillver** and **reflionx**. First, **DAO** includes a more complete and up-to-date atomic database than that of **reflionx**. Second, **DAO** implements a more accurate treatment of Compton scattering than the current **xillver** and **reflionx** tables (see Figures 3 and 4). Third, **DAO** is open-source and allows users to freely define their own incident spectrum. This flexibility is crucial for several applications—for example, modeling returning radiation (Mirzaev et al. 2024a,b), or describing reflection in Z sources where the illuminating spectrum is neither a pure power law nor a blackbody, but

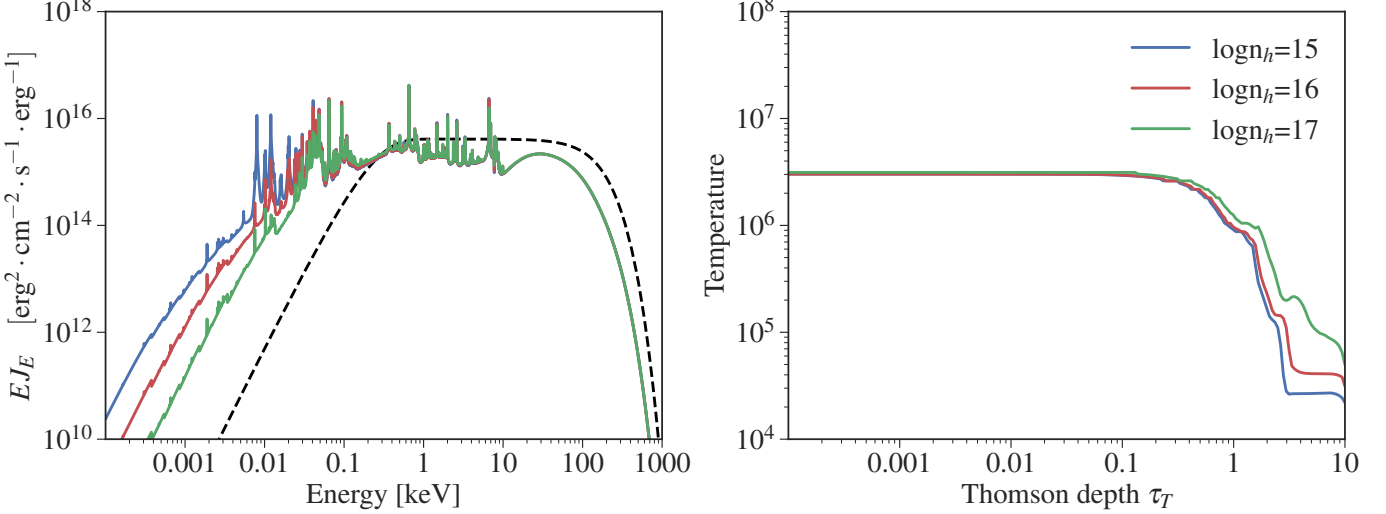


Figure 13. Angle-averaged reflection spectra for different hydrogen densities, normalized relative to the spectrum at $\log n_h = 15$. Since the ionizing flux F_x is proportional to the hydrogen density n_h (Eq. 2), the spectra for $\log n_h = 16$ and 17 are scaled by factors of 10 and 100, respectively. All other parameters are the same as the default values listed in Table 1.

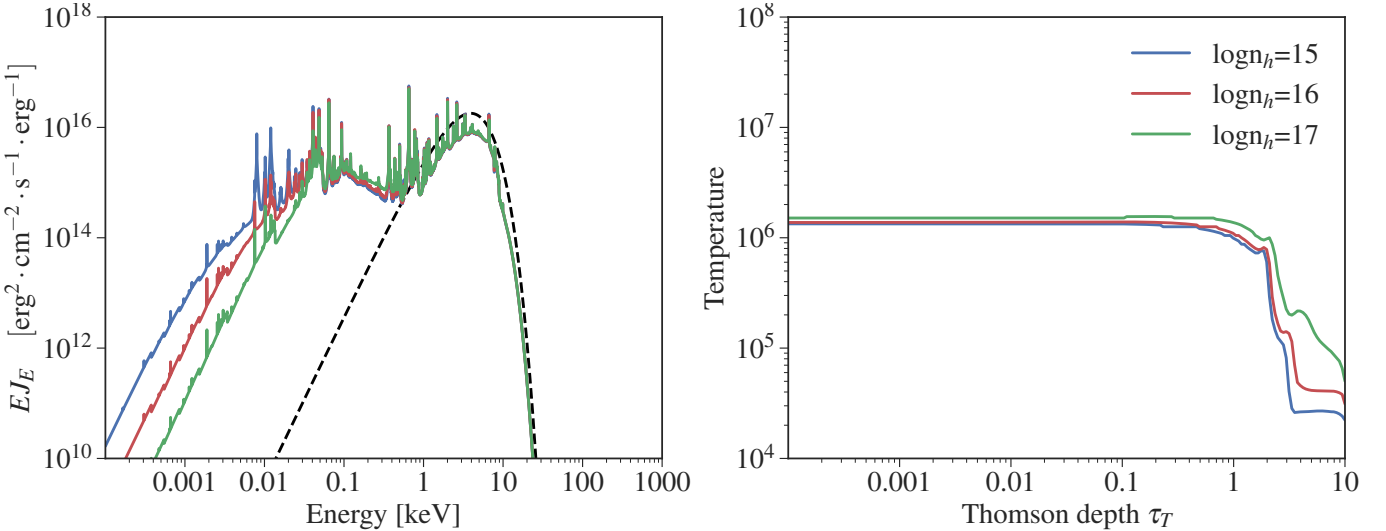


Figure 14. Consistent with the setup in Figure 13, the incident radiation in this plot is modeled as a blackbody with $kT_{bb} = 1$ keV.

instead a saturated Comptonization continuum (Ludlam 2024).

In the future, we plan to extend our model to higher hydrogen densities to better represent environments with dense gas in XRBs and AGNs (e.g., Jiang et al. 2019; Liu et al. 2023a), and to incorporate disk-blackbody radiation from the bottom boundary, which is particularly important for X-ray binaries (e.g., Ross & Fabian 2007). We will also implement a non-uniform vertical density structure and account for hydrostatic equilibrium (Done & Nayakshin 2007). Another major development will be the inclusion of polarization in the radiative transfer calculations, including Compton scattering for polarized X-ray reflection spectra. We fur-

ther intend to examine the impact of different atomic databases and photoionization codes, for example by integrating CLOUDY (Gunasekera et al. 2025) into our framework.

Acknowledgments – We sincerely thank Ekaterina Sokolova-Lapa and Yuanze Ding for their insightful comments and generous assistance throughout the preparation of this paper. This work was supported by the National Natural Science Foundation of China (NSFC), Grant No. W2531002. HL acknowledges support from The Gruber Foundation fellowship. AI acknowledges support by the European Union (ERC, X-MAPS, 101169908). Views and opinions expressed are however those of the author(s) only and do not necessar-

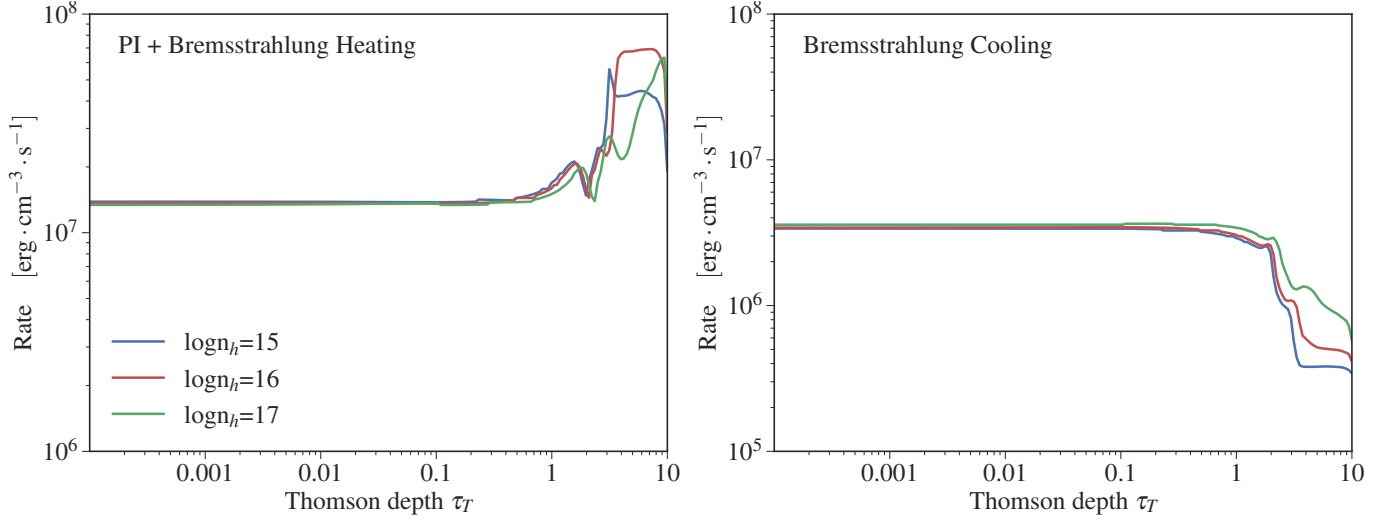


Figure 15. Photoionization and bremsstrahlung heating rates, along with the bremsstrahlung cooling rate, corresponding to the reflection spectra shown in Figure 14.

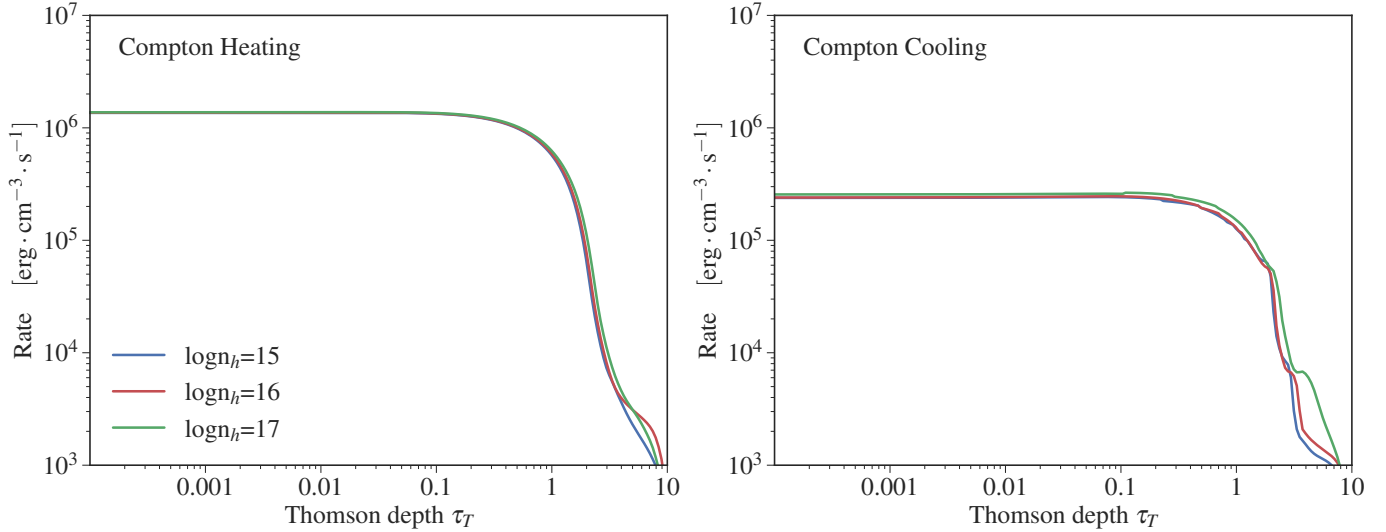


Figure 16. Compton heating and cooling rates, corresponding to the reflection spectra shown in Figure 14.

ily reflect those of the European Union or the European

Research Council. Neither the European Union nor the granting authority can be held responsible for them.

REFERENCES

- Arnaud, K. A. 1996, in Astronomical Society of the Pacific Conference Series, Vol. 101, Astronomical Data Analysis Software and Systems V, ed. G. H. Jacoby & J. Barnes, 17
- Auer, L. 1967, ApJL, 150, L53, doi: [10.1086/180091](https://doi.org/10.1086/180091)
- Ballantyne, D. R., Ross, R. R., & Fabian, A. C. 2001, MNRAS, 327, 10, doi: [10.1046/j.1365-8711.2001.04432.x](https://doi.org/10.1046/j.1365-8711.2001.04432.x)
- Bambi, C. 2024, arXiv e-prints, arXiv:2408.12262, doi: [10.48550/arXiv.2408.12262](https://doi.org/10.48550/arXiv.2408.12262)
- Bambi, C., Brenneman, L. W., Dauser, T., et al. 2021, SSRv, 217, 65, doi: [10.1007/s11214-021-00841-8](https://doi.org/10.1007/s11214-021-00841-8)
- Buisson, D. J. K., Fabian, A. C., Barret, D., et al. 2019, MNRAS, 490, 1350, doi: [10.1093/mnras/stz2681](https://doi.org/10.1093/mnras/stz2681)
- Dauser, T., García, J. A., Joyce, A., et al. 2022, MNRAS, 514, 3965, doi: [10.1093/mnras/stac1593](https://doi.org/10.1093/mnras/stac1593)
- Dauser, T., Wilms, J., Reynolds, C. S., & Brenneman, L. W. 2010, MNRAS, 409, 1534, doi: [10.1111/j.1365-2966.2010.17393.x](https://doi.org/10.1111/j.1365-2966.2010.17393.x)

- Ding, Y., Garcia, J. A., Kallman, T. R., et al. 2024, ApJ, 974, 280, doi: [10.3847/1538-4357/ad76a1](https://doi.org/10.3847/1538-4357/ad76a1)
- Done, C., & Nayakshin, S. 2007, MNRAS, 377, L59, doi: [10.1111/j.1745-3933.2007.00303.x](https://doi.org/10.1111/j.1745-3933.2007.00303.x)
- Draghis, P. A., Miller, J. M., Costantini, E., et al. 2024, ApJ, 969, 40, doi: [10.3847/1538-4357/ad43ea](https://doi.org/10.3847/1538-4357/ad43ea)
- Dumont, A. M., Abrassart, A., & Collin, S. 2000, A&A, 357, 823, doi: [10.48550/arXiv.astro-ph/0003220](https://doi.org/10.48550/arXiv.astro-ph/0003220)
- Dumont, A.-M., Collin, S., Paletou, F., et al. 2003, A&A, 407, 13, doi: [10.1051/0004-6361:20030890](https://doi.org/10.1051/0004-6361:20030890)
- Fabian, A. C., Rees, M. J., Stella, L., & White, N. E. 1989, MNRAS, 238, 729, doi: [10.1093/mnras/238.3.729](https://doi.org/10.1093/mnras/238.3.729)
- Feautrier, P. 1964, Comptes Rendus Academie des Sciences (serie non specifiee), 258, 3189
- . 1967, Annales d'Astrophysique, 30, 125
- . 1968, Annales d'Astrophysique, 31, 257
- García, J., Dauser, T., Reynolds, C. S., et al. 2013, ApJ, 768, 146, doi: [10.1088/0004-637X/768/2/146](https://doi.org/10.1088/0004-637X/768/2/146)
- García, J., & Kallman, T. R. 2010, ApJ, 718, 695, doi: [10.1088/0004-637X/718/2/695](https://doi.org/10.1088/0004-637X/718/2/695)
- García, J., Kallman, T. R., & Mushotzky, R. F. 2011, ApJ, 731, 131, doi: [10.1088/0004-637X/731/2/131](https://doi.org/10.1088/0004-637X/731/2/131)
- García, J., Dauser, T., Lohfink, A., et al. 2014, ApJ, 782, 76, doi: [10.1088/0004-637X/782/2/76](https://doi.org/10.1088/0004-637X/782/2/76)
- García, J. A., Dauser, T., Ludlam, R., et al. 2022, ApJ, 926, 13, doi: [10.3847/1538-4357/ac3cb7](https://doi.org/10.3847/1538-4357/ac3cb7)
- García, J. A., Fabian, A. C., Kallman, T. R., et al. 2016, MNRAS, 462, 751, doi: [10.1093/mnras/stw1696](https://doi.org/10.1093/mnras/stw1696)
- García, J. A., Sokolova-Lapa, E., Dauser, T., et al. 2020, ApJ, 897, 67, doi: [10.3847/1538-4357/ab919b](https://doi.org/10.3847/1538-4357/ab919b)
- George, I. M., & Fabian, A. C. 1991, MNRAS, 249, 352, doi: [10.1093/mnras/249.2.352](https://doi.org/10.1093/mnras/249.2.352)
- Grevesse, N., Noels, A., & Sauval, A. J. 1996, in Astronomical Society of the Pacific Conference Series, Vol. 99, Cosmic Abundances, ed. S. S. Holt & G. Sonneborn, 117
- Guilbert, P. W. 1981, MNRAS, 197, 451, doi: [10.1093/mnras/197.2.451](https://doi.org/10.1093/mnras/197.2.451)
- Gunasekera, C. M., van Hoof, P. A. M., Dehghanian, M., et al. 2025, arXiv e-prints, arXiv:2508.01102, doi: [10.48550/arXiv.2508.01102](https://doi.org/10.48550/arXiv.2508.01102)
- Huang, Y., Liu, H., Cosimo, B., et al. 2025, DAO: A New Reflection Model, Zenodo, doi: [10.5281/zenodo.17839597](https://doi.org/10.5281/zenodo.17839597)
- Huang, Y., Liu, H., Mirzaev, T., et al. 2025, ApJ, 989, 168, doi: [10.3847/1538-4357/adf111](https://doi.org/10.3847/1538-4357/adf111)
- Hubeny, I., & Mihalas, D. 2015, Theory of Stellar Atmospheres: An Introduction to Astrophysical Non-equilibrium Quantitative Spectroscopic Analysis (Princeton, NJ: Princeton University Press)
- Jiang, J., Gallo, L. C., Fabian, A. C., Parker, M. L., & Reynolds, C. S. 2020, MNRAS, 498, 3888, doi: [10.1093/mnras/staa2625](https://doi.org/10.1093/mnras/staa2625)
- Jiang, J., Fabian, A. C., Dauser, T., et al. 2019, MNRAS, 489, 3436, doi: [10.1093/mnras/stz2326](https://doi.org/10.1093/mnras/stz2326)
- Kallman, T., & Bautista, M. 2001, ApJS, 133, 221, doi: [10.1086/319184](https://doi.org/10.1086/319184)
- Kallman, T., Bautista, M., Deprince, J., et al. 2021, ApJ, 908, 94, doi: [10.3847/1538-4357/abccd6](https://doi.org/10.3847/1538-4357/abccd6)
- Kara, E., García, J. A., Lohfink, A., et al. 2017, MNRAS, 468, 3489, doi: [10.1093/mnras/stx792](https://doi.org/10.1093/mnras/stx792)
- Lightman, A. P., Lamb, D. Q., & Rybicki, G. B. 1981, ApJ, 248, 738, doi: [10.1086/159198](https://doi.org/10.1086/159198)
- Lightman, A. P., & White, T. R. 1988, ApJ, 335, 57, doi: [10.1086/166905](https://doi.org/10.1086/166905)
- Liu, H., Abdikamalov, A. B., Mirzaev, T., et al. 2025, MNRAS, 536, 2594, doi: [10.1093/mnras/stae2722](https://doi.org/10.1093/mnras/stae2722)
- Liu, H., Jiang, J., Zhang, Z., et al. 2023a, ApJ, 951, 145, doi: [10.3847/1538-4357/acd8b9](https://doi.org/10.3847/1538-4357/acd8b9)
- Liu, H., Bambi, C., Jiang, J., et al. 2023b, ApJ, 950, 5, doi: [10.3847/1538-4357/acca17](https://doi.org/10.3847/1538-4357/acca17)
- Ludlam, R. M. 2024, Ap&SS, 369, 16, doi: [10.1007/s10509-024-04281-y](https://doi.org/10.1007/s10509-024-04281-y)
- Madej, J., Różańska, A., Majczyna, A., & Należyty, M. 2017, MNRAS, 469, 2032, doi: [10.1093/mnras/stx994](https://doi.org/10.1093/mnras/stx994)
- Magdziarz, P., & Zdziarski, A. A. 1995, MNRAS, 273, 837, doi: [10.1093/mnras/273.3.837](https://doi.org/10.1093/mnras/273.3.837)
- Mendoza, C., Bautista, M. A., Palmeri, P., et al. 2017, A&A, 604, A63, doi: [10.1051/0004-6361/201730724](https://doi.org/10.1051/0004-6361/201730724)
- . 2018, A&A, 616, A62, doi: [10.1051/0004-6361/201832939](https://doi.org/10.1051/0004-6361/201832939)
- Mendoza, C., Bautista, M. A., Deprince, J., et al. 2021, Atoms, 9, 12, doi: [10.3390/atoms9010012](https://doi.org/10.3390/atoms9010012)
- Mihalas, D. 1978, Stellar Atmospheres (San Francisco: W. H. Freeman and Company)
- Milkey, R. W., Shine, R. A., & Mihalas, D. 1975, ApJ, 202, 250, doi: [10.1086/153971](https://doi.org/10.1086/153971)
- Mirzaev, T., Bambi, C., Abdikamalov, A. B., et al. 2024a, ApJ, 976, 229, doi: [10.3847/1538-4357/ad8a63](https://doi.org/10.3847/1538-4357/ad8a63)
- Mirzaev, T., Riaz, S., Abdikamalov, A. B., et al. 2024b, ApJ, 965, 66, doi: [10.3847/1538-4357/ad303b](https://doi.org/10.3847/1538-4357/ad303b)
- Molendi, S., Bianchi, S., & Matt, G. 2003, MNRAS, 343, L1, doi: [10.1046/j.1365-8711.2003.06783.x](https://doi.org/10.1046/j.1365-8711.2003.06783.x)
- Morrison, R., & McCammon, D. 1983, ApJ, 270, 119, doi: [10.1086/161102](https://doi.org/10.1086/161102)
- Nagirner, D. I., & Poutanen, Y. J. 1993, Astronomy Letters, 19, 262
- Nayakshin, S., Kazanas, D., & Kallman, T. R. 2000, ApJ, 537, 833, doi: [10.1086/309054](https://doi.org/10.1086/309054)

- Novikov, I. D., & Thorne, K. S. 1973, in *Black Holes (Les Astres Occlus)*, ed. C. DeWitt & B. S. DeWitt (New York: Gordon and Breach Science Publishers), 343–450
- Paletou, F., & Auer, L. H. 1995, *A&A*, 297, 771
- Pomraning, G. C. 1973, The equations of radiation hydrodynamics
- Poutanen, J., & Svensson, R. 1996, *ApJ*, 470, 249, doi: [10.1086/177865](https://doi.org/10.1086/177865)
- Poutanen, J., Veledina, A., & Zdziarski, A. A. 2018, *A&A*, 614, A79, doi: [10.1051/0004-6361/201732345](https://doi.org/10.1051/0004-6361/201732345)
- Poutanen, J., & Vurm, I. 2010, *ApJS*, 189, 286, doi: [10.1088/0067-0049/189/2/286](https://doi.org/10.1088/0067-0049/189/2/286)
- Reynolds, C. S. 2021, *ARA&A*, 59, 117, doi: [10.1146/annurev-astro-112420-035022](https://doi.org/10.1146/annurev-astro-112420-035022)
- Riaz, S., Szanecki, M., Niedźwiecki, A., Ayzenberg, D., & Bambi, C. 2021, *ApJ*, 910, 49, doi: [10.3847/1538-4357/abe2a3](https://doi.org/10.3847/1538-4357/abe2a3)
- Risaliti, G., Harrison, F. A., Madsen, K. K., et al. 2013, *Nature*, 494, 449, doi: [10.1038/nature11938](https://doi.org/10.1038/nature11938)
- Ross, R. R., & Fabian, A. C. 1993, *MNRAS*, 261, 74, doi: [10.1093/mnras/261.1.74](https://doi.org/10.1093/mnras/261.1.74)
- . 2005, *MNRAS*, 358, 211, doi: [10.1111/j.1365-2966.2005.08797.x](https://doi.org/10.1111/j.1365-2966.2005.08797.x)
- . 2007, *MNRAS*, 381, 1697, doi: [10.1111/j.1365-2966.2007.12339.x](https://doi.org/10.1111/j.1365-2966.2007.12339.x)
- Ross, R. R., Weaver, R., & McCray, R. 1978, *ApJ*, 219, 292, doi: [10.1086/155776](https://doi.org/10.1086/155776)
- Schuster, A. 1905, *ApJ*, 21, 1, doi: [10.1086/141186](https://doi.org/10.1086/141186)
- Shakura, N. I., & Sunyaev, R. A. 1973, *A&A*, 24, 337
- Shapiro, S. L., Lightman, A. P., & Eardley, D. M. 1976, *ApJ*, 204, 187, doi: [10.1086/154162](https://doi.org/10.1086/154162)
- Suchy, S., Fürst, F., Pottschmidt, K., et al. 2012, *ApJ*, 745, 124, doi: [10.1088/0004-637X/745/2/124](https://doi.org/10.1088/0004-637X/745/2/124)
- Suleimanov, V., Poutanen, J., & Werner, K. 2012, *A&A*, 545, A120, doi: [10.1051/0004-6361/201219480](https://doi.org/10.1051/0004-6361/201219480)
- Tanaka, Y., Nandra, K., Fabian, A. C., et al. 1995, *Nature*, 375, 659, doi: [10.1038/375659a0](https://doi.org/10.1038/375659a0)
- Tarter, C. B., Tucker, W. H., & Salpeter, E. E. 1969, *ApJ*, 156, 943, doi: [10.1086/150026](https://doi.org/10.1086/150026)
- Thorne, K. S., & Price, R. H. 1975, *ApJL*, 195, L101, doi: [10.1086/181720](https://doi.org/10.1086/181720)
- Tripathi, A., Nampalliwar, S., Abdikamalov, A. B., et al. 2019a, *ApJ*, 875, 56, doi: [10.3847/1538-4357/ab0e7e](https://doi.org/10.3847/1538-4357/ab0e7e)
- Tripathi, A., Zhang, Y., Abdikamalov, A. B., et al. 2021, *ApJ*, 913, 79, doi: [10.3847/1538-4357/abf6cd](https://doi.org/10.3847/1538-4357/abf6cd)
- Tripathi, A., Yan, J., Yang, Y., et al. 2019b, *ApJ*, 874, 135, doi: [10.3847/1538-4357/ab0a00](https://doi.org/10.3847/1538-4357/ab0a00)
- Zdziarski, A. A., Johnson, W. N., Done, C., Smith, D., & McNaron-Brown, K. 1995, *ApJL*, 438, L63, doi: [10.1086/187716](https://doi.org/10.1086/187716)
- Zdziarski, A. A., Johnson, W. N., & Magdziarz, P. 1996, *MNRAS*, 283, 193, doi: [10.1093/mnras/283.1.193](https://doi.org/10.1093/mnras/283.1.193)
- Zdziarski, A. A., Lubiński, P., Gilfanov, M., & Revnivtsev, M. 2003, *MNRAS*, 342, 355, doi: [10.1046/j.1365-8711.2003.06556.x](https://doi.org/10.1046/j.1365-8711.2003.06556.x)
- Zhang, S.-N., Li, T., Lu, F., et al. 2020, *Science China Physics, Mechanics, and Astronomy*, 63, 249502, doi: [10.1007/s11433-019-1432-6](https://doi.org/10.1007/s11433-019-1432-6)
- Życki, P. T., Done, C., & Smith, D. A. 1999, *MNRAS*, 309, 561, doi: [10.1046/j.1365-8711.1999.02885.x](https://doi.org/10.1046/j.1365-8711.1999.02885.x)

APPENDIX

A. ALGORITHM

The second-order radiative transfer equation is given by

$$\mu^2 \frac{\partial^2 u_{\mu\nu}}{\partial \tau_\nu^2} = u_{\mu\nu} + S_\nu \quad (\text{A1})$$

The derivatives with respect to optical depth can be approximated using finite differences as

$$\left(\frac{dX}{d\tau} \right)_{d-\frac{1}{2}} = \frac{X_d - X_{d-1}}{\tau_d - \tau_{d-1}}, \quad \left(\frac{dX}{d\tau} \right)_{d+\frac{1}{2}} = \frac{X_{d+1} - X_d}{\tau_{d+1} - \tau_d} \quad (\text{A2})$$

and the second derivative at depth index d is approximated by

$$\left(\frac{d^2 X}{d\tau^2} \right)_d \approx \frac{(dX/d\tau)_{d+\frac{1}{2}} - (dX/d\tau)_{d-\frac{1}{2}}}{\frac{1}{2} (\Delta\tau_{d+\frac{1}{2}} + \Delta\tau_{d-\frac{1}{2}})} \quad (\text{A3})$$

In this discretization, the derivative operator is applied to the spatial grid, while the energy and angle dependencies are treated implicitly. Defining the optical depth intervals as $\Delta\tau_{d+1/2} = \tau_{d+1} - \tau_d$ and $\Delta\tau_{d-1/2} = \tau_d - \tau_{d-1}$, the centered interval is given by

$$\Delta\tau_d = \frac{1}{2} (\Delta\tau_{d-\frac{1}{2}} + \Delta\tau_{d+\frac{1}{2}}) \quad (\text{A4})$$

Let m and n denote the angle and energy indices, respectively. The discrete form of Eq. A1 within the domain defined by $\tau_{\min} < \tau < \tau_{\max}$, $\mu_{\min} \leq \mu \leq \mu_{\max}$, and $\nu_{\min} \leq \nu \leq \nu_{\max}$ is expressed as:

$$\frac{\mu_m^2 u_{d-1,m,n}}{\Delta\tau_{d-\frac{1}{2},n} \Delta\tau_{d,n}} - \frac{\mu_m^2 u_{d,m,n}}{\Delta\tau_{d,n}} \left(\frac{1}{\Delta\tau_{d-\frac{1}{2},n}} + \frac{1}{\Delta\tau_{d+\frac{1}{2},n}} \right) + \frac{\mu_m^2 u_{d+1,m,n}}{\Delta\tau_{d+\frac{1}{2},n} \Delta\tau_{d,n}} = u_{d,n} - S_{d,n} \quad (\text{A5})$$

At the upper boundary, the intensity u at the second depth point ($d = 2$) can be expanded using a Taylor series around the surface ($d = 1$):

$$u_2 = u_1 + \Delta\tau_{\frac{3}{2}} \left(\frac{du}{d\tau} \right)_{d=1} + \frac{1}{2} \Delta\tau_{\frac{3}{2}}^2 \left(\frac{d^2 u}{d\tau^2} \right)_{d=1} \quad (\text{A6})$$

Substituting this expansion into Eq. A1 yields

$$\mu \frac{u_2 - u_1}{\Delta\tau_1} = u_1 + \Delta\tau_1 \frac{u_1 - S_1}{2\mu} + I_{\text{inc}}. \quad (\text{A7})$$

A similar procedure is applied to the lower boundary. Combining these boundary conditions with Eqs. A5 and A7 results in a block tridiagonal system of the form

$$-A_d u_{d-1} + B_d u_d - C_d u_{d+1} = R_d, \quad 2 \leq d \leq ND - 1 \quad (\text{A8})$$

In Eq. A8, the subscripts denoting angle and energy are omitted for clarity. At the two boundaries, $d = 1$ and $d = ND$, the coronal illumination I_{inc} and the disk self-emission I_{bb} must be included in the source terms. Generally, I_{inc} is anisotropic and depends on the physical properties of the corona, while I_{bb} is an isotropic, multi-temperature blackbody spectrum. Eq. A8 can be reformulated in a compact vector notation as:

$$\mathbf{T} \cdot \mathbf{u} = \mathbf{R}, \quad (\text{A9})$$

where \mathbf{T} represents the coefficient matrix, \mathbf{u} is the vector of mean intensities, and \mathbf{R} is the corresponding source vector. Equation A9, together with the boundary condition in Eq. A7, is solvable via a recursive forward-elimination

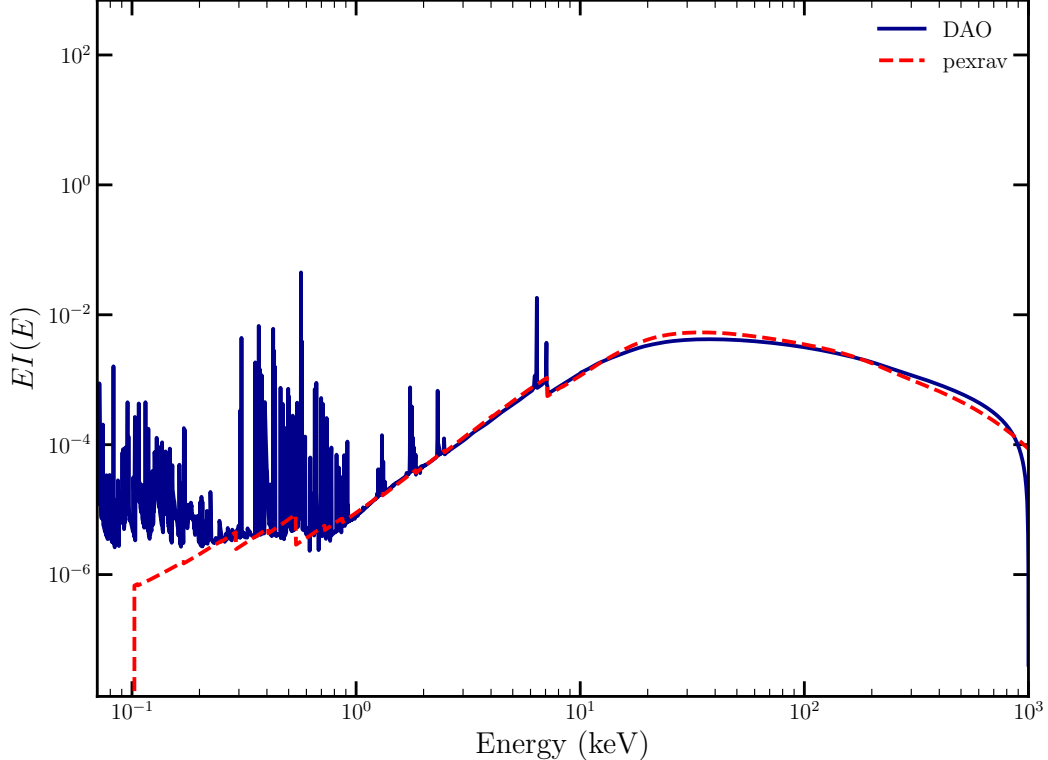


Figure 17. The illuminating continuum is a cut-off power law with a high-energy cut-off of $E_{\text{cut}} = 1000$ keV. For the DAO model, the material is set to be neutral by fixing the ionization parameter at $\log \xi = 0.0$. We adopt a standard iron abundance of $A_{\text{Fe}} = 1.0$ and set the abundances of nickel, calcium, and argon to zero ($A_{\text{Ni}} = 0.0$, $A_{\text{Ca}} = 0.0$, $A_{\text{Ar}} = 0.0$) to expedite the calculation. The other parameters in DAO are set at default values.

and back-substitution procedure (Feautrier 1964, 1967, 1968). This solution scheme is collectively known as the Feautrier method.

We validate our radiative transfer code by comparing its results with the established reflection model **pexrav** (Magdziarz & Zdziarski 1995), as illustrated in Figure 17. The spectra presented in Figure 17 demonstrate excellent agreement in the continuum below 10 keV. While the **pexrav** spectrum exhibits a slightly higher peak in the Compton Hump range, the two models agree well at energies $E < 20$ keV and $E > 50$ keV. We hypothesize that this difference will decrease upon the inclusion of the angle-dependent source function, as described in Section 2. It must be noted that the **pexrav** model does not incorporate line emission; however, this exclusion is negligible when focusing on the high-energy scattered continuum.

B. COMPTON SCATTERING REDISTRIBUTION FUNCTION

B.1. Gaussian approximation redistribution function

The Gaussian redistribution function was first applied to the scattering problem in Compton-thick atmospheres by Ross et al. (1978); Ross & Fabian (1993) to describe the down-scattering of photons with $E < 200$ keV, and was later extended by Nayakshin et al. (2000) to treat Compton scattering over the full energy range.

This redistribution function describes the probability that a photon with initial energy E_i is scattered to energy E_f :

$$P(E_i, E_f) = \frac{1}{\sqrt{2\pi}\Sigma} \exp \left[-\frac{(E_f - E_c)^2}{2\Sigma^2} \right], \quad (\text{B10})$$

with the central energy E_c and standard deviation Σ defined as

$$E_c = E_i \left(1 + \frac{4kT}{m_e c^2} - \frac{E_i}{m_e c^2} \right), \quad (\text{B11})$$

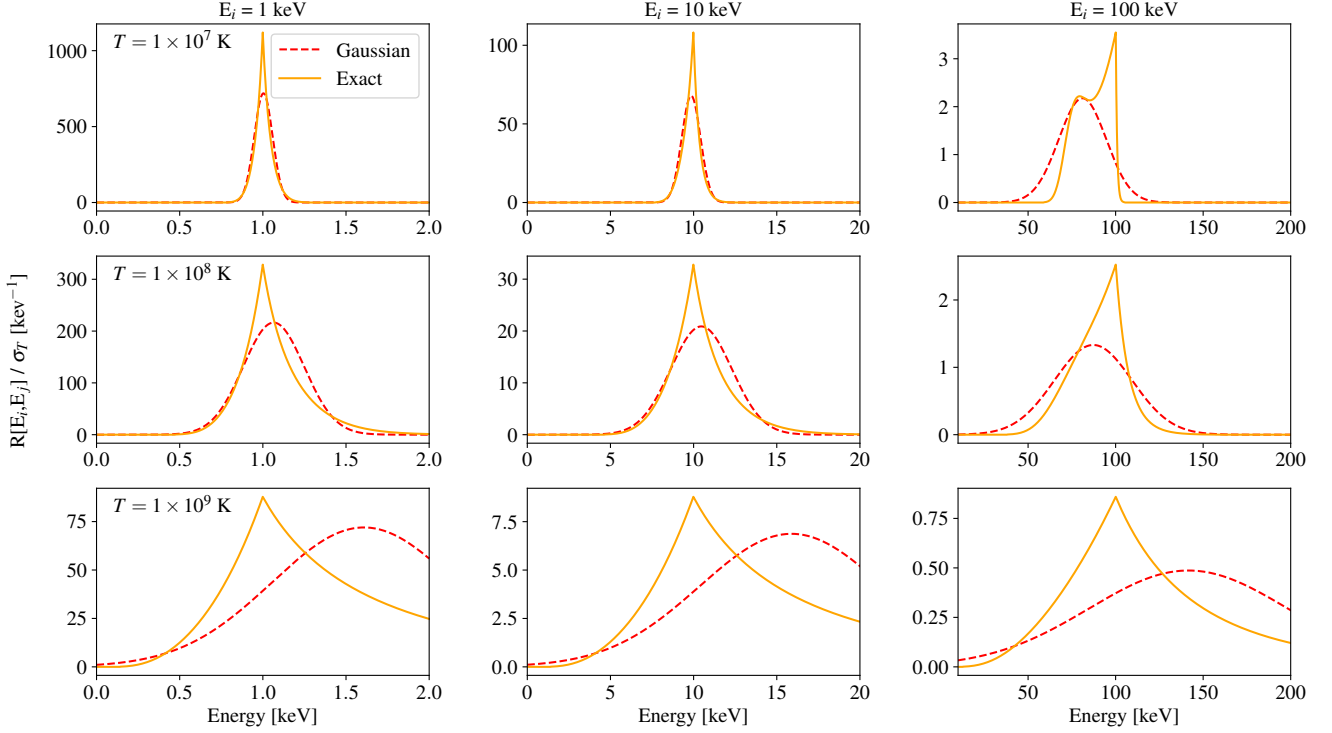


Figure 18. Gaussian (red dash line) and Exact redistribution (orange solid line) function with three initial energy: $E_i = 1, 10, 100$ keV and three different gas temperature: $10^7, 10^8, 10^9$ K.

and

$$\Sigma = E_i \left[\frac{2kT}{m_e c^2} + \frac{2}{5} \left(\frac{E_i}{m_e c^2} \right)^2 \right]^{1/2}. \quad (\text{B12})$$

B.2. Exact Redistribution Function

We adopt the exact redistribution function following the formalism of Nagirner & Poutanen (1993) and Nayakshin et al. (2000):

$$R_E(x, x_1, \mu, \gamma) = \frac{2}{Q} + \frac{u}{v} \left(1 - \frac{2}{q} \right) + u \frac{(u^2 - Q^2)(u^2 + 5v)}{2q^2 v^3} + u \frac{Q^2}{q^2 v^2}, \quad (\text{B13})$$

where x and x_1 represent the dimensionless photon energies before and after scattering, respectively, μ is the cosine of the scattering angle, and γ denotes the electron Lorentz factor. Here, $q = x x_1 (1 - \mu)$ and $Q^2 = (x - x_1)^2 + 2q$, while the auxiliary variables are defined as

$$a_-^2 = (\gamma - x)^2 + \frac{1 + \mu}{1 - \mu}, \quad a_+^2 = (\gamma + x_1)^2 + \frac{1 + \mu}{1 - \mu}, \quad (\text{B14})$$

and

$$v = a_- a_+, \quad u = a_+ - a_-. \quad (\text{B15})$$

The redistribution function averaged over a relativistic Maxwellian distribution is given by

$$R(x, x_1, \mu) = \frac{3}{32\mu\Theta K_2(1/\Theta)} \int_{(x-x_1+Q\sqrt{1+2/q})/2}^{\infty} R_E(x, x_1, \mu, \gamma) \exp(-\gamma/\Theta) d\gamma, \quad (\text{B16})$$

where K_2 is the modified Bessel function of the second kind and $\Theta = kT/m_e c^2$. In this work, the angle-averaged redistribution is employed; thus, the resulting function is

$$R(x, x_1) = \int_{\mu_{\min}}^{\mu_{\max}} R(x, x_1, \mu) d\mu. \quad (\text{B17})$$

Figure 18 illustrates the significant deviation between the exact redistribution function and the Gaussian approximation when the gas temperature is high and the photon energies are large. Similar results were reported by García et al. (2020); the comparison is reproduced here to facilitate the reader’s understanding of the differences. The redistribution function in Eq. B17 satisfies the normalization condition with respect to the Compton scattering cross section:

$$\frac{\sigma_{\text{cs}}(E)}{\sigma_T} = \int_0^\infty R(E_i, E_f) dE_f. \quad (\text{B18})$$

Rather than the Klein–Nishina cross section, σ_{KN} , the Compton scattering cross section averaged over a relativistic Maxwellian electron distribution, denoted by σ_{cs} , is employed:

$$\begin{aligned} \sigma_{\text{cs}}(x) = \frac{3\sigma_T}{16x^2\Theta K_2(1/\Theta)} \int_1^\infty e^{-\gamma/\Theta} \left\{ \left(x\gamma + \frac{9}{2} + \frac{2\gamma}{x} \right) \ln \left[\frac{1+2x(\gamma+z)}{1+2x(\gamma-z)} \right] - 2xz \right. \\ \left. + z \left(x - \frac{2}{x} \right) \ln(1+4x\gamma+4x^2) + \frac{4x^2z(\gamma+x)}{1+4x\gamma+4x^2} \right. \\ \left. - 2 \int_{x(\gamma-z)}^{x(\gamma+z)} \ln(1+2\varepsilon) \frac{d\varepsilon}{\varepsilon} \right\} d\gamma. \end{aligned} \quad (\text{B19})$$

A detailed comparison between σ_{cs} and σ_{KN} is provided in García et al. (2020).

C. RELATIVISTIC SPECTRUM

The `reldao` and `reldaoA` models are developed within the framework of `relxill` v2.5 (García et al. 2014; Huang et al. 2025) and `relxillA` (Huang et al. 2025). Currently, as the full table models have not yet been generated, `reldao` serves as a prototype rather than a finalized relativistic reflection model. The code will be publicly released upon the completion of the DAO table models. Additionally, the relativistic spectrum is computed using the convolution model `relconv` (Dauser et al. 2010) within `XSPEC` (Arnaud 1996), yielding the combined model `relconv*dao`.

The primary distinction between the convolution model `relconv*dao` and the direct implementations, `reldao` and `reldaoA`, lies in the treatment of angular dependence. The convolution model operates on the angle-averaged flux, whereas `reldao` accounts for the full angular distribution by integrating over all local emission angles at a given incidence angle. Furthermore, `relxillA` incorporates a more comprehensive treatment of angular effects. In the specific case of `reldao`, the observed flux is calculated as

$$F_{\text{obs}}(E_{\text{obs}}) = \frac{1}{D^2} \int_{R_{in}}^{R_{out}} dr_e \int_0^1 g^* \frac{\pi r_e g^2}{\sqrt{g^*(1-g^*)}} \left[f^{(1)}(g^*, r_e, \theta_{\text{obs}}) + f^{(2)}(g^*, r_e, \theta_{\text{obs}}) \right] \times \epsilon(r_e) \langle \bar{I}_e(E_e) \rangle \quad (\text{C20})$$

and for `reldaoA`, the model calculates the observed flux as

$$\begin{aligned} F_{\text{obs}}(E_{\text{obs}}) = \frac{1}{D^2} \sum_{i=0}^9 \int_{R_{in}}^{R_{out}} dr_e \int_0^1 dg^* \frac{\pi r_e g^2}{\sqrt{g^*(1-g^*)}} \left[f^{(1)}(g^*, r_e, \theta_{\text{obs}}) + f^{(2)}(g^*, r_e, \theta_{\text{obs}}) \right] \\ \times \epsilon(r_e) \bar{I}(E_e, r_e, \theta_e) \Theta(\theta_e - \theta_i) \Theta(\theta_{i+1} - \theta_e) \end{aligned} \quad (\text{C21})$$

All the physical parameters above have been explained in detail in section 2 of Huang et al. (2025). The relativistic reflection spectra are presented in Figure 19. Each spectrum is normalized by its total flux, according to $F(E) = F(E) / \int F(E) dE$. The `reldao` and `reldaoA` models yield consistent results, whereas the convolution model, `relconv*dao`, exhibits marked deviations in both the Compton hump region and the soft X-ray band.

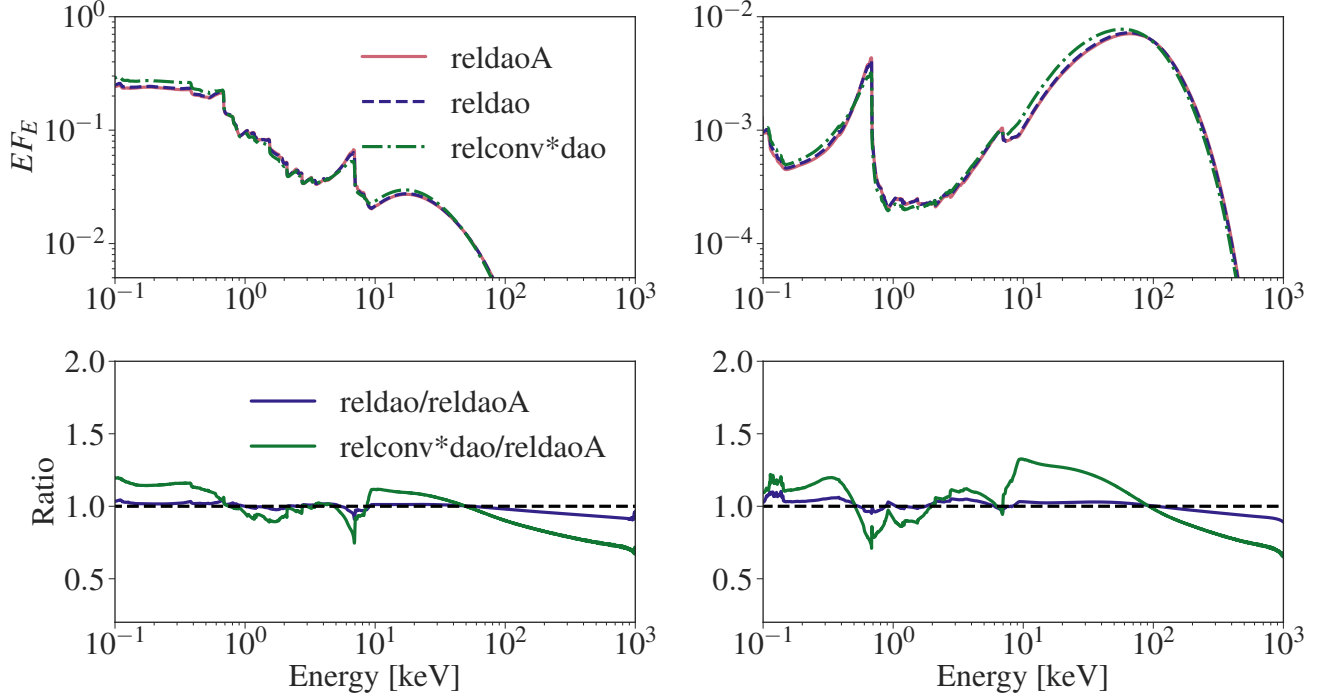


Figure 19. Relativistic reflection spectra calculated with `relconv*dao` (green dash-dot line), `reldao` (blue dashed line), and `reldaoA` (red solid line). The gas is illuminated by `nthcomp` with $\Gamma = 2.4$ (left column) and $\Gamma = 1.4$ (right column). Ionization parameter is set to 3.0 for both cases. The inclination angle is $\theta_i = 30$ deg, and all other parameters in `relxill` are fixed at their default values.